

We are IntechOpen, the world's leading publisher of Open Access books Built by scientists, for scientists

6,300

Open access books available

171,000

International authors and editors

190M

Downloads

Our authors are among the

154

Countries delivered to

TOP 1%

most cited scientists

12.2%

Contributors from top 500 universities



WEB OF SCIENCE™

Selection of our books indexed in the Book Citation Index
in Web of Science™ Core Collection (BKCI)

Interested in publishing with us?
Contact book.department@intechopen.com

Numbers displayed above are based on latest data collected.
For more information visit www.intechopen.com



Application of Microfluidics in Biosensors

Jing Wang, Yong Ren and Bei Zhang

Abstract

This chapter reviews the up-to-date researches in the field of biosensors integrated with microfluidic techniques, most of which are publications within the last 5 years. The features of these biosensors, their applications, challenges, and possible future research interests in this field are also reviewed.

Keywords: microfluidics, biosensor, bioreceptor, lab-on-a-chip, bioaffinity, PDMS, μ PAD, paper-based microfluidics, electrochemistry, optics, surface plasmon resonance, colorimetric, fluorescent, cell culture, food safety

1. Introduction

Biosensors are defined, by Tudos and Schasfoort [1], as “analytical devices comprised of a biological element (tissue, microorganism, organelle, cell receptor, enzyme, antibody) and a physicochemical transducer. Specific interaction between the target analyte and the biological material produces a physico-chemical change detected by the transducer. The transducer then yields an analog electronic signal proportional to the amount (concentration) of a specific analyte or group of analytes” [1]. The features of biosensors include the bio-recognition unit and the transduction mechanism from biological signals to measurable electronic signals, e.g., color, current, voltage, capacitance, light intensity, wavelength, and phase. Major parameters to assess the performances of biosensors include the following:

- High sensitivity. The sensitivity of a biosensor is always the first and one of the most important parameters in assessing its performance. The efficiency in capturing analytes, the specific characterization of the analyte, the capability of converting biological signals into electronic signals (or the response of the system), and the systematic and environmental noises both determine the sensitivity of a biosensor.
- High stability and repeatability. The stability of a biosensor refers to the capability of a biosensor in performing consistently and reliably under designated environments, and the stability of a biosensor is especially important when assessing portable or wearable biosensors that usually are applied in scenarios involving varied temperature, velocity, humidity, pressure, lighting conditions, etc. The repeatability of a biosensor mainly refers to the long-term performance of a biosensor under the same conditions and is usually tested regularly in commercial biosensors in order to recalibration.

- Quick response or real-time analysis and diagnosis. Real-time analysis usually delivers more information than providing a final result, e.g., binding rate, reaction time, kinetics, and saturation conditions, which can serve for the analysis in the applications of biological and chemical reactions and drug analysis. Response time required to bind sufficient molecules upon the sensing surface is typically determined by diffusion, which can extend to hours and even to days to generate a signal above the background noise level. This applies fundamentally to all sensors that accumulate and concentrate target molecules onto a transducer, including fluorophore-tagged molecules in microarray spots, label-free optical biosensors, and impedance-based sensors [2].
- Low consumption of sample volume. The samples for biosensors are usually with low volume due to the nature, e.g., tissue, antibody, and some biological samples are with low concentration or small molecular weight, and this enforces biosensors to perform with minimum sample consumption.
- Ease of operation. The application of biosensors goes from laboratory-based research to commercially available devices for at-home use. The operation of biosensors should eliminate professional operation or understanding of the device, but simply involves collecting samples and reading results.
- High throughput. Single-function biosensors are fading away from stage even with extremely low cost. Biosensors should be able to integrate all the good qualities mentioned in above bullet points together with the capability of multiple-tasking.

In traditional clinical healthcare, interests are in high-quality biosensor for the measurement of physiological indices. With the development in the requests of Internet of Things and self-service techniques, the interests and emphasis in healthcare transfers from clinical healthcare to family healthcare, e.g., long-term monitoring of chronic disease [3], disease prevention and early detection, reachable clinical services for remote districts, etc. Under the precondition of high quality, biosensors miniaturized as portable or wearable are emerging to meet the new trend of era, which promise a bright future in health management and digital health; researches on the biological and instrumental parts of point-of-care (POC) and lab-on-a-chip (LOC) techniques belong to this area. The potential applications of biosensors include real-time health monitoring, remotely synchronizing health data with medical personnel, patient management, POC disease diagnosis, big data statistics in health management, etc. [4]. Real-time health monitoring in domestic applications enables patients to monitor the health status by themselves at home without the assistance of professional personnel at minimum cost. Health data synchronized with medical personnel spares the patients from transporting and waiting for outpatient services, saving time and reducing medical expenses. Based on the collected health data, a potential service of clinical diagnosis is possible in an artificial intelligent health system in the near future [5]. Meanwhile, these new applications impose more requirements on the researches and developments of biosensors, as stated below.

- Low cost. For at-home applications, lower cost of biosensors is vital, so there are emerging researches on adopting cheap materials, simplifying sensing systems and adopting smart phones in data processing, etc.
- Noninvasive collection of samples. Biosensors for sensing human samples, noninvasive sensing, is preferable, especially for everyday or frequent

measurements. Researches using human samples as saliva, tear, sweat, and urine are one of the hottest topics.

- Miniaturization of the biosensing systems [4, 5], including sample pre-processing unit, sensing unit, data collection/processing system, and data displaying unit.
- The design of integrated sensor chip. A sensor chip with multiple functions is preferable especially for sensing human samples.

2. Challenges in biosensing technologies

All the qualities mentioned above, which both researchers and industry are seeking for, raise multiple challenges, and we try to summarize and list below:

- **Specific binding.** The recognition of analytes should be specific only to the analytes which is not affected by other chemicals, molecules, or cells. This is significantly more challenging when the sample components are complex and mixed with various kinds of molecules. For example, the detection of one specific antibody in human blood sample should eliminate the effects of all other antibodies, cells, electrolytes, etc., the detection reflects only the concentration of this antibody, and the detection of one specific heavy metal ion in a real polluted water sample should be able to distinguish the reaction induced by all other ions.
- **Non-specific binding, i.e., biofouling,** in some cases significantly introduces signal noise, drift, or delay in biosensors [6]. The most common method to reduce non-specific binding is to completely wash the binding surface with buffer after the binding processing is finished; thus the weak binding induced by non-specific binding could be eliminated to the minimum extent.
- **Properties of bioreceptors, e.g., concentration and alignment.** Plenty of papers [3, 7–10] presented the protocols of surface activation, modification, and functionalization, but the protocols greatly depend on operation and environment. Even following exactly the same protocol, the coverage rate of bioreceptors and the repeatability of operation may vary a lot, due to the immobilization of multiple layers on the sensor surface, which usually involves linking layers for stable sensor surfaces like gold and silicon, so the surface treatment protocols should be tested before operating the binding events. So far quite limited number of papers presented theoretical and/or experimental analysis on the effect of bioreceptor alignment/orientation on the performance of biosensors. The linking layer molecules are usually randomly polarized and oriented, which can induce destructive interference and dramatically reduce the collective charge polarization [11], and this means that even the surface treatment protocols could be repeated and the alignment of bioreceptors is another parameter that will highly affect the outcomes of the binding events. The detection becomes less sensitive. Chu [12] proposed a method to homogenize the orientation of the chemical linker on nanowire-based field-effect sensor by applying an external voltage on a metal plate about 1 mm above the chip surface at certain frequency while grounding the back gate electrode; thus the molecular conformation can be maintained for hours or longer, and this method has been tested and proven by the detection of DNA hybridization

reactions with poly-15 T ssDNA, showing that the alignment process promotes the sensitivity by 10-fold.

- Design of biosensor assay matrix. The effects of specific and non-specific binding on signal was tested and analyzed by Schneider [13, 14], which proves that for all the binding events, proper design of the sensor assay should be optimized, especially when the sample components is complex, for example, proper reference binding sites should be included in order to eliminate non-specific binding from different components. But this in another way increased the requirement in both the imaging capability of the biosensor and the data processing capability. Meanwhile, the surface treatment, modification, and functionalization [4, 7, 9, 10, 15, 16] will be more complicated and need to be tested and verified, and the complexity in sensor surface properties (e.g., various refractive indices of bioreceptors) requests better system compatibility and responsivity.
- Low concentration target molecule within a low-volume sample, i.e., extremely limited number of analytes available for detection. For the example, in the research of POC and LOC, 20–50 μL finger prick blood contains over 20,000 kinds of biomarkers of clinical interest at concentrations as low as 10 pg./mL , meaning that only 106–107 available biomolecules for one target [2].

3. What is microfluidics?

The definition of microfluidics, given by Whitesides from Harvard University, is: It is the science and technology of systems that process or manipulate small amounts (10^{-9} to 10^{-18} liters) of fluids, using channels with dimensions of tens to hundreds of micrometers. It offers fundamentally new capabilities in the control of concentrations of molecules in space and time [17].

The material most commonly adopted for the fabrication of microfluidic structures is poly-dimethylsiloxane (PDMS), which is optically transparent and able to support important microfluidic components, e.g., pneumatic valves; meanwhile there are other materials with research interests, e.g., polycarbonate, polyolefin, silicon, and glass. Recently paper-based (reviews by [3, 18–21], and research by [22–28]) and cloth-based [29] microfluidics are drawing more attention because of the low cost, easy fabrication, and lightweight which are essential properties for POC applications. The major features of microfluidics are the small consumption of liquid sample and tiny dimensions of structures, which have significant impact on the development of biosensors, so the integration of microfluidics into biosensing techniques complies with the development of the era and generates unique features in biosensors, e.g., trace level of sample at high sensitivity.

4. Advantages of microfluidic-integrated biosensors

Microfluidics provide a closed and stable biosensing environment so to improve sensitivity. For on-site portable biosensors, the effect of an open environment on sensing results hugely lowers the biosensor performance. By integrating the microfluidic structures, sample processing and biosensing reactions are carried out within a closed and relatively stable environment, thus promising better sensitivity and reliability [30]. Taking the example of the application of solid-phase polymerase chain reaction (SP-PCR) in online molecular diagnosis, the

development of this technique is hindered by lack of sensitive and portable on-chip optical detection technology. Hung [24] proposed a LOC device which combined the solid-phase polymerase chain reaction with supercritical angle fluorescence (SAF) microlens array embedded in a microchip. He demonstrated a high sensitivity of 1.6 copies/ μL and showed comparable detection limit and linear range to off-chip detection using conventional laser scanner, and he stated this device as an on-chip highly sensitive and multiplexed pathogen detection with low-cost and compact optical components.

Microfluidic channel can efficiently, accurately, and significantly reduce the sensing area. Simulations and experiment results have shown that reducing the sensing area could shorten sensing time and increase the sensitivity with smaller sample requirement, especially at lower target concentrations [7, 11]. An increase in sensitivity of two orders of magnitude has been reported by Li et al. [31]. Meanwhile, the distribution of binding events along the sensing surface could be heterogeneous, and this could be induced by the heterogeneous in bioreceptor coverage, different alignment of bioreceptors, nonuniform concentrations of targets within samples in laminar flow, and nonuniform temperature, pressure, or other physical parameters along the sensing surface, the heterogeneity can be eliminated to minimum. Reduced sensing area also means miniaturizing sample volume which is essentially valuable to low concentration targets and rare targets with limited access.

Microfluidic structures are capable of integrating multiple functions within one device without introducing extra equipment or tools. For example, by designing and optimizing microfluidic channels, sample injection, pretreatment, and processing can be easily realized. Usually for biosensing, the modification of the biosensing surface is compulsory for specific binding of targets, and this is doable in microfluidic structures which are even more stable and more promising than manual operations. For the biosensing events, the volume and speed control of sample are achievable which provides more valuable information, e.g., binding affinity, binding rate, kinetics, etc.

Microfluidic devices are capable of automation. With or without external pumping system/equipment/tools, microfluidics is capable of integrating sample pre- and post-processing, sensing, surface modification, temperature control, EM field control, etc. The automation of microfluidic-integrated sensors and structures is reviewed by [30, 32–34]. However, the automation of whole microfluidic-integrated biosensor as one device still seems quite challenging as the liquid handling in this field is usually more complex which could involve up to dozens of solutions and operations like filtering, centrifugation, etc., together with the activity of biological samples to be considered. Partially automatized microfluidic-integrated DNA biosensors are reviewed by Ansari [35]. Joung [36] presented a novel lateral flow immunosensor (LFI) for microfluidic-integrated enzyme immunosorbent assay (EIA) in POC testing (POCT), a chemiluminescent LFI-based automatic EIA system, the operation of which does not require additional steps such as mechanical fluidic control, washing, or injecting. The key concept relies on a delayed-release effect of chemiluminescent substrates (luminol enhancer and hydrogen peroxide generator) by an asymmetric polysulfone membrane (ASPM). When the ASPM was placed between the nitrocellulose membrane and the substrate pad, substrates encapsulated in the substrate pad were released after 5.3 ± 0.3 min. As a proof of concept, the high-sensitivity C-reactive protein level in human serum was detected by this sensor.

Microfluidics enables both separate and mutual processing of multiple binding assays with single or multiple samples simultaneously. For the detection of single or multiple targets in a real or complex solution, the design of the binding assay usually involves more than one kind of bioreceptors, thus meaning

that the designed samples to flow over each bioreceptor spot could be different. The delivering of different kinds of samples in sequential orders can be realized by unique design of microfluidic channels, pneumatic valves [17, 37], and/or centrifugal forces [33, 34].

Microfluidic structures ensure the precise control over experimental conditions [38]. What can be precisely controlled by microfluidic structures include flow rate, sample volume, channel volume, channel height, reaction time, etc. Integration of sensors with microfluidic channels serves to reduce assay time by constraining the diffusion distance between the molecules in the sample and the sensor and to create laminar flow over the sensor to distribute target molecules broadly and uniformly [2].

5. The present of microfluidic-integrated biosensors

Biosensors can be classified based on target recognition events and transduction mechanisms [4]. Based on the target recognition events, biosensor receptors are included. Based on the transduction mechanisms, biosensors can be classified into optical biosensor (Raman scattering [39–44], surface plasmon resonance (SPR) [6, 45–47], fiber Bragg grating [48–53], fluorescent [54–58], chemiluminescence [36, 59]), electrochemical biosensor [60–64], calorimetric biosensor [6, 22, 65–69], and piezoelectric biosensor [70–74].

5.1 Target recognition

Biological targets to be detected by biosensors, especially for the detection of analytes holden by human beings/animals, could be divided into two kinds, i.e., physical parameters and physiological/biological targets. Physical parameters like the body temperature, blood pressure, heart rate, velocity, and location usually do not request a corresponding and unique bioreceptor on the biosensor, as these physical parameters usually can be detected directly by optical, electronic, and piezoelectric sensors. Analytes as physiological/biological targets, however, cannot be detected directly, because of the complex components in a real human sample, so bioreceptors are adopted for the specific recognition of these targets, including cell, antibodies, DNAs, aptamers, and molecularly imprinted polymers [4].

The most commonly adopted physiological fluids of human beings/animals are blood, which has to be collected in an invasive way, and fluids that can be collected in a noninvasive way, e.g., sweat, saliva, tears, and urine, can be used in the prediction and diagnosis of various diseases [75–77]. Comparing with other physiological fluids, saliva is the outstanding fluid with the advantages of easy accessing and large volume, but with a major disadvantage of large range of variability in components and concentrations depending on the extent of oral cleanliness; examples that have been experimentally verified are using human saliva for the detection of cytokine [78], dopamine [51], insulin [79], fetuin [80], bacterial load [81], cholesterol [25], and cortisol [82]; using tear for the detection of dopamine [83], proteomic, lipidomic, and metabolomic composition [77]; using sweat for the detection of cytokine [84] and proteomic [76]; and using urine for the detection of anticancer drugs [85], L-carnitine [86], *Chlamydia trachomatis*, and *Neisseria gonorrhoeae* [87]. Samples of sweat and tear have been significantly undeveloped until quite recent when flexible materials and flexible electronic techniques achieved some milestones [4]. Currently the most well-explored targets in human physiological fluids include electrolytes (e.g., K^+ , Ca^{2+} , Na^+) and major metabolites (e.g., myocardial enzyme,

glucose, urea), which lack specification to diseases, indicating the general physiological conditions [4].

5.2 Transduction mechanism

So far, optical biosensors deliver the best sensitivity among the three other kinds of biosensors; electrochemical biosensors are the most popular choice as commercial-potential biosensors because of the compact size, low cost, and acceptable sensitivity; colorimetric biosensors are with a distinguished advantage of easy operation at extremely low cost but with a major disadvantage of low sensitivity; while the researches on piezoelectric biosensors are quite limited comparing with three other kinds of biosensors. Some most up-to-date researches on all four kinds of biosensors are presented below.

5.2.1 Optical biosensors

Surface-enhanced Raman spectroscopy (SERS) and surface plasmon resonance are the two powerful optical biosensors with a unique feature of label-free sensing, as the analytes need no pre-processing to be labeled before sensing events and thus eliminate the false-positive or false-negative biosensing results induced by the labels. The first commercial product of SPR biosensor appeared in 1990 by the company of Pharmacia (named Biacore afterwards). Since then, more than 1000 papers were published annually using commercial SPR biosensors [88]. Most of these commercial SPR biosensors are bulky and only laboratory based. The development of plasmonic-based biosensors in the field of POC was reviewed in [43] together with recent advances in surface chemistry, substrate fabrication, and microfluidic integration. Here we explore a bit wider which is not limited to POC but microfluidic-integrated biosensors. In most of the researches mentioned below, the microfluidic structure usually serves as the sample handling unit.

Tunc I et al. [39] presented the molecular specificity of Raman spectroscopy together with self-assembled monolayer of metallic AuNPs to detect CA125 antibody-antigen molecules. Highly enhanced electromagnetic fields localized around neighboring AuNPs provide hot-spot construction due to the spatial distribution of SERS enhancement on the CA125 proteins at nM concentration level.

Carneiro M et al. [41] reported the detection of carcinoembryonic antigen (CEA) in SERS using two different bioreceptors for CEA, i.e., a molecularly imprinted polymer (MIP) and a natural antibody. The MIP acted as a pre-concentration scheme for the CEA, while the natural antibody signals the presence of CEA on the MIP platform. The MIP film was first incubated in the sample containing CEA and next incubated in SERS tag, which is gold nano-stars coupled to 4-aminothiophenol (4-ATP) as Raman reporter, so the MIP acted as a pre-concentration scheme for the CEA. Then the MIP was exposed to the natural CAE antibody. A sensitivity down to 1.0 ng/mL was reported.

Zhu JY et al. [89] presented a biosensor that can be used for clinical diagnosis. This biosensor is based on localized surface plasmon resonance integrated with a biomimetic microfluidic “adipose-tissue-on-chip” platform for an in situ label-free, high-throughput, and multiplexed cytokine secretion analysis of obese adipose tissue. It was stated that this system enables simultaneous measurements of pro-inflammatory (IL-6 and TNF-alpha) and anti-inflammatory (IL-10 and IL-4) cytokines secreted by the adipocytes and macrophages and identified stage-specific cytokine secretion profiles from a complex milieu during obesity progression.

In the research of [90], the plasmonic biosensor integrated the microfluidic unit for plasma separation, allows the in-line separation of plasma directly from the bloodstream without any pre-processing outside the device, and channels it to the active detection area, where inorganic cerium oxide nanoparticles function as local selective dopamine binding sites through strong surface redox reaction. A detection limit of dopamine was achieved at 100 fM concentration in simulated body fluid and 1 nM directly from blood without any prior sample preparation. This demonstration shows the feasibility of the practical implementation of the proposed plasmonic system in detection of a variety of biomarkers directly from the complex biological fluids. Li XK et al. [91] reported the plasmonic biosensor integrated a multifunctional microfluidic system with small-volume microchamber and regulation channels for reliable monitoring of cytokine secretion from individual cells for hours.

Besides the traditional plasmonic materials, graphene has recently received more and more attention in the field of both labeled and label-free sensing, because of its ability to harness electromagnetic fields, strong light-matter interaction of graphene layer, and its highly tunable optical properties [40]. Liu HP et al. [40] simulated the detection capacity of the graphene plasmonic biosensor using three-dimensional finite difference time domain method. Numerical results showed that the maximum sensitivity and figure of merit of the biosensor are 333.3 nm/RIU and 16.665 RIU, respectively.

Fluorescence is the other powerful optical biosensor which labels analytes and promises high sensitivity and specificity in target recognition. Raducanu VS et al. [56] reported a direct fluorescent signal transducer embedded in a DNA aptamer for versatile metal-ion detection. This sensor embedded with guanine-rich DNA aptamer internally coupled with Cy3 fluorescent dye that measures directly the DNA conformational changes upon metal-ion binding. Our signal transducer is environmentally sensitive that is internally coupled to the DNA aptamer. Potassium ion concentration was successfully measured in a variety of aqueous and biological test samples.

5.2.2 Electrochemical biosensors

There are plenty of researches on electrochemical biosensors, and majority of the commercialized biosensors belong to this category. Here we only present the electrochemical biosensors integrated with microfluidics that possesses both miniaturized structure and high sensitivity.

Electrode-based chemolectrical biosensors are the most common ones. Usually a working electrode and a blank/reference electrode are designed in such biosensor, and the samples cover both electrodes and generate a measurable electrical signal. Mi SL et al. [92] reported a sensitivity up to 567 nA mM⁽⁻¹⁾ mm⁽⁻²⁾, and the limit of detection was 4.5 M (vs. Ag/AgCl as the reference electrode) in the detection of metabolic lactate concentrations in HepG2 cells cultured with cancer drugs.

Evans D et al. [93] demonstrated a fully integrated microfluidic amperometric enzyme-linked immunosorbent assay prototype using a commercial interferon gamma release assay as a model antibody binding system. What is unique in this research is that the assay cell is based on a printed circuit board (PCB) and the microfluidic assay chemistry was engineered to take place on the Au-plated electrodes within the cell. All components were manufactured exclusively via standard commercial PCB fabrication processes. A detection limit comparable to high-end commercial systems and a short diagnosis time of 8 minutes were demonstrated.

Silicon nanowire field-effect transistor is one of the most sensitive biosensing techniques, but it is limited to analytes that carry charges. Weakly charged or uncharged analytes can hardly be detected [11]. Evans D et al. [31] presented a

method of immobilizing bioreceptors on the silicon nanowire sensing surface only, comparing with the traditional methods in which a large surrounding substrate is also covered with bioreceptors, and it was proven that restricting the surface modification substantially improves the sensitivity.

Besides silicon nanowire, copper nanowire is adopted in electrochemical biosensors [94]. In [94], microfluidic chip is coupled to copper nanowires for the fast diagnosis of galactosemia in precious newborn urine samples. Galactosemia is a rare disease that is diagnosed through the identification of different metabolite profiles. The specific detection of galactose 1-phosphate (Gal 1-P), galactose (Gal), and uridyl diphosphate galactose (UDP-Gal) confirms type I, II, and III galactosemia diseases. The detection is extremely fast which is less than 350 s, required negligible urine sample consumption, and displayed impressive signal-to-noise characteristics and excellent reproducibility.

Oliveira MC et al. [95] presented an amperometric biosensor using a screen-printed electrode modified with carbon nanotubes and nickel ions for the detection of glucose, which is characterized by the chemical oxidation of carbohydrate by NiOOH. Under optimized conditions, a limit of detection 3.9 $\mu\text{mol/L}$ and a limit of quantification of 13 $\mu\text{mol/L}$ were reported. The effect of concomitant species such as ascorbic acid, dopamine, and uric acid was investigated, and this method was successfully applied for the determination of glucose in a commercial blood serum human (original and spiked) sample. What is unique in this research is that the microfluidic system was assembled on a 3D-printed platform constructed with acrylonitrile butadiene styrene and integrated with nine cotton threads, providing a stable flow rate.

5.2.3 Colorimetric biosensors

Plenty of reports are available on colorimetric biosensors integrated with microfluidics, e.g., [27, 28, 96–98]; most of the reports highlighted the features of cost-effectiveness and miniaturization. Different from three other kinds of biosensors, the materials adopted for the integrated microfluidic structures are usually not PDMS, but paper for the majority and cloth in some researches. Currently majority of the researches focus on the applications in food safety [22, 27, 96] and heavy metal detection [67, 99, 100] in aqueous environment. The researches in the application of biological analytes are quite limited, due to the natures of analytes and bioreceptors and the environment conditions in order to keep the activities of both analytes and bioreceptors.

Fraser LA et al. [101] presented a malaria biosensor whereby aptamers are coated onto magnetic microbeads for magnet-guided capture, wash, and detection of the biomarker. A biosensor incorporating three separate microfluidic chambers was designed to enable such magnet-guided equipment-free colorimetric detection of PfLDH. The biosensor showed high sensitivity and specificity when detecting PfLDH using both in vitro cultured parasite samples and clinical samples from malaria patients.

5.2.4 Piezoelectric biosensors

The research of piezoelectric biosensor integrated with microfluidics is quite underdeveloped so far. Possible reasons could be the lower sensitivity, poor biocompatibility, and complicated fabrication.

Yamaguchi M. [82] proposed a mass sensor based on mechanical resonance that incorporates a disk-shaped mechanical resonator, a separate piezoelectric element used to excite vibrations in the resonator, and a microfluidic mechanism. Electrical

power is used to actuate the piezoelectric element, leaving the resonator free from power lines. This sensor was reported to be suitable to analyze the concentration of a salivary hormone, cortisol in human saliva samples.

6. Future research interests

Future possible research interests in the field of microfluidic-integrated biosensors are proposed as the following:

- Exploration of materials for both microfluidics and nanofluidics in different application scenarios. Besides PDMS, the exploration of other materials, e.g., engineering polymers, traditional glass, silicon, or metal, in special applications that requires high chemical stability, high thermal stability, unique optical properties, and/or special mechanical properties.
- Fabrication of microfluidics and nanofluidics and structures (e.g., valves, mixers).
- Microfluidics with high chemical and thermal stability for special applications.
- Integration of microfluidics and nanofluidics with sensors to form complete and functional systems that require no professional operations and ease in applications, e.g., LOC, etc.
- Integration of microfluidics with data processing algorithms. The application of machine learning in sensing data processing could enhance the performance of biosensors in specialized environments.
- Integration of microfluidics with communication techniques. Synchronization of sensing data with relevant users, remote control of the biosensors, and big data analysis of special sensing networks can be realized.

7. Conclusions

The state-of-the-art advances in biosensor development based on microfluidic technology have been reviewed in the book chapter with focus on the applications, challenges, and possible future research interests for each type of biosensor. It can be envisioned that microfluidic-based biosensors will remain a hot topic of investigations because of the ever-increasing demands in various applications ranging from industry to biomedical detection. The interests in microfluidic-integrated biosensors promise even more prospective future in these areas. It is applications in wearable biosensor; portable biosensor can be explored in the future with enhanced sensitivity, improved stability, and miniaturized structure.

Acknowledgements

This research was supported by Zhejiang Provincial Natural Science Foundation of China under Grant No. LQ19F050003 as well as Ningbo Science and Technology Bureau under Service Industry Science & Technology Programme with project code 2019F1030.

Conflict of interest

The authors declare no conflict of interest.

IntechOpen

Author details

Jing Wang^{1*}, Yong Ren² and Bei Zhang^{3*}

1 Department of Electrical and Electronic Engineering, University of Nottingham Ningbo China, Zhejiang, China

2 Department of Mechanical, Materials and Manufacturing Engineering, University of Nottingham Ningbo China, Zhejiang, China

3 Department of Automation Science and Electrical Engineering, Beihang University, Beijing, China

*Address all correspondence to: jing.wang@nottingham.edu.cn;
bei.zhang@buaa.edu.cn

IntechOpen

© 2020 The Author(s). Licensee IntechOpen. Distributed under the terms of the Creative Commons Attribution - NonCommercial 4.0 License (<https://creativecommons.org/licenses/by-nc/4.0/>), which permits use, distribution and reproduction for non-commercial purposes, provided the original is properly cited. 

References

- [1] Schasfoort RBM, Tudos AJ. Handbook of Surface Plasmon Resonance. Royal Soc Chemistry; 2008
- [2] Che C et al. Activate capture and digital counting (AC + DC) assay for protein biomarker detection integrated with a self-powered microfluidic cartridge. *Lab on a Chip*. 2019;**19**(23):3943-3953
- [3] Vashist SK et al. Emerging technologies for next-generation point-of-care testing. *Trends in Biotechnology*. 2015;**33**(11):692-705
- [4] Tu J et al. The Era of Digital Health: A Review of Portable and Wearable Affinity Biosensors. *Advanced Functional Materials*. 2019:1906713
- [5] Steinhubl SR, Muse ED, Topol EJ. The emerging field of mobile health. *Science Translational Medicine*. 2015;**7**(283):283rv3
- [6] Wang J et al. Highly sensitive multipoint real-time kinetic detection of surface plasmon bioanalytes with custom CMOS cameras. *Biosensors and Bioelectronics*. 2014;**58**:157-164
- [7] Ciampi S, Harper JB, Gooding JJ. Wet chemical routes to the assembly of organic monolayers on silicon surfaces via the formation of Si-C bonds: Surface preparation, passivation and functionalization. *Chemical Society Reviews*. 2010;**39**(6):2158-2183
- [8] Liang G et al. Fiber Optic Surface Plasmon Resonance-Based Biosensor Technique: Fabrication, Advancement, and Application. *Critical Reviews in Analytical Chemistry*. 2016:213-223
- [9] Mok J et al. Digital microfluidic assay for protein detection. *Proceedings of the National Academy of Sciences*. 2014;**111**(6):2110-2115
- [10] Sun J, Wang S, Gao F. Covalent surface functionalization of semiconducting polymer dots with beta-cyclodextrin for fluorescent Ratiometric assay of cholesterol through host-guest inclusion and FRET. *Langmuir*. 2016;**32**(48):12725-12731
- [11] Shen M-Y, Li B-R, Li Y-K. Silicon nanowire field-effect-transistor based biosensors: From sensitive to ultra-sensitive. *Biosensors and Bioelectronics*. 2014;**60**:101-111
- [12] Chu CJ et al. Improving nanowire sensing capability by electrical field alignment of surface probing molecules. *Nano Letters*. 2013;**13**(6):2564-2569
- [13] Schneider CS et al. Surface plasmon resonance as a high throughput method to evaluate specific and non-specific binding of nanotherapeutics. *Journal of Controlled Release*. 2015;**219**:331-344
- [14] Wuethrich A, Howard CB, Trau M. Geometric optimisation of electrohydrodynamic fluid flows for enhanced biosensing. *Microchemical Journal*. 2018;**137**:231-237
- [15] Arreola J et al. Surface functionalization for spore-based biosensors with organosilanes. *Electrochimica Acta*. 2017;**241**:237-243
- [16] Platt GW et al. Allergen immobilisation and signal amplification by quantum dots for use in a biosensor assay of IgE in serum. *Biosensors and Bioelectronics*. 2014;**52**:82-88
- [17] Whitesides GM. The origins and the future of microfluidics. *Nature*. 2006;**442**(7101):368-373
- [18] Mross S et al. Microfluidic enzymatic biosensing systems: A review. *Biosensors and Bioelectronics*. 2015;**70**:376-391

- [19] Yetisen AK, Akram MS, Lowe CR. Paper-based microfluidic point-of-care diagnostic devices. *Lab on a Chip*. 2013;**13**(12):2210-2251
- [20] Li X, Ballerini DR, Shen W. A perspective on paper-based microfluidics: Current status and future trends. *Biomicrofluidics*. 2012;**6**(1):011301
- [21] Nie Z et al. Integration of paper-based microfluidic devices with commercial electrochemical readers. *Lab on a Chip*. 2010;**10**(22):3163-3169
- [22] Aksorn J, Teepoo S. Development of the simultaneous colorimetric enzymatic detection of sucrose, fructose and glucose using a microfluidic paper-based analytical device. *Talanta*. 2020;**207**:120302
- [23] Chethana K et al. Fiber bragg grating sensor based device for simultaneous measurement of respiratory and cardiac activities. *Journal of Biophotonics*. 2017;**10**(2):278-285
- [24] Hung TQ et al. A novel lab-on-chip platform with integrated solid phase PCR and supercritical angle fluorescence (SAF) microlens array for highly sensitive and multiplexed pathogen detection. *Biosensors and Bioelectronics*. 2017;**90**:217-223
- [25] Lee YJ et al. Enzyme-loaded paper combined impedimetric sensor for the determination of the low-level of cholesterol in saliva. *Sensors and Actuators B: Chemical*. 2018;**271**:73-81
- [26] López Marzo AM et al. All-integrated and highly sensitive paper based device with sample treatment platform for Cd²⁺ immunodetection in drinking/tap waters. *Analytical Chemistry*. 2013;**85**(7):3532-3538
- [27] Mooltongchun M, Teepoo S. A simple and cost-effective microfluidic paper-based biosensor analytical device and its application for hypoxanthine detection in meat samples. *Food Analytical Methods*. 2019;**12**(12):2690-2698
- [28] Rafatmah E, Hemmateenejad B. Colorimetric and visual determination of hydrogen peroxide and glucose by applying paper-based closed bipolar electrochemistry. *Microchimica Acta*. 2019;**186**(11)
- [29] Guan W, Liu M, Zhang CS. Electrochemiluminescence detection in microfluidic cloth-based analytical devices. *Biosensors & Bioelectronics*. 2016;**75**:247-253
- [30] Alam MK et al. Recent advances in microfluidic technology for manipulation and analysis of biological cells (2007-2017). *Analytica Chimica Acta*. 2018;**1044**:29-65
- [31] Li B-R et al. Biomolecular recognition with a sensitivity-enhanced nanowire transistor biosensor. *Biosensors and Bioelectronics*. 2013;**45**:252-259
- [32] Maceiczuk RM, Lignos IG, DeMello AJ. Online detection and automation methods in microfluidic nanomaterial synthesis. *Current Opinion in Chemical Engineering*. 2015;**8**:29-35
- [33] Burger R, Amato L, Boisen A. Detection methods for centrifugal microfluidic platforms. *Biosensors and Bioelectronics*. 2016;**76**:54-67
- [34] Torres Delgado SM et al. Wirelessly powered and remotely controlled valve-array for highly multiplexed analytical assay automation on a centrifugal microfluidic platform. *Biosensors and Bioelectronics*. 2018;**109**:214-223
- [35] Ansari MIH et al. Microfluidic-integrated DNA nanobiosensors.

Biosensors and Bioelectronics.
2016;**85**:247-260

[36] Joung H-A, Oh YK, Kim M-G. An automatic enzyme immunoassay based on a chemiluminescent lateral flow immunosensor. *Biosensors and Bioelectronics*. 2014;**53**:330-335

[37] Pradeep A et al. Automated and programmable electromagnetically actuated valves for microfluidic applications. *Sensors and Actuators a-Physical*. 2018;**283**:79-86

[38] Halldorsson S et al. Advantages and challenges of microfluidic cell culture in polydimethylsiloxane devices. *Biosensors and Bioelectronics*. 2015;**63**:218-231

[39] Tunc I, Susapto HH. Label-free detection of ovarian Cancer antigen CA125 by surface enhanced Raman scattering. *Journal of Nanoscience and Nanotechnology*. 2020;**20**(3):1358-1365

[40] Liu HP et al. A 3D multilayer curved plasmonic coupling array with abundant and uniform hot spots for surface-enhanced Raman scattering. *Journal of Physics D: Applied Physics*. 2020;**53**(5)

[41] Carneiro M et al. Dual biorecognition by combining molecularly-imprinted polymer and antibody in SERS detection. Application to carcinoembryonic antigen. *Biosensors & Bioelectronics*. 2019:146

[42] Lee T et al. Single functionalized pRNA/gold nanoparticle for ultrasensitive MicroRNA detection using electrochemical surface-enhanced Raman spectroscopy. *Advanced Science*.

[43] Li ZH et al. Plasmonic-based platforms for diagnosis of infectious diseases at the point-of-care. *Biotechnology Advances*. 2019;**37**(8):107440

[44] Sakir M et al. Photocatalytic green fabrication of Au nanoparticles on ZnO nanorods modified membrane as flexible and photocatalytic active reusable SERS substrates. *Colloids and Surfaces a-Physicochemical and Engineering Aspects*. 2020;**585**

[45] Bhardwaj H, Sumana G, Marquette CA. A label-free ultrasensitive microfluidic surface Plasmon resonance biosensor for Aflatoxin B1 detection using nanoparticles integrated gold chip. *Food Chemistry*. 2020;**307**:125530

[46] Das CM et al. A theoretical insight into the use of anti-reflective coatings for the upliftment of sensitivity of surface plasmon resonance sensors. *Optics Communications*. 2020;**458**

[47] Farmani H, Farmani A, Biglari Z. A label-free graphene-based nanosensor using surface plasmon resonance for biomaterials detection. *Physica E-Low-Dimensional Systems & Nanostructures*. 2020;**116**

[48] Chen XY et al. In-situ detection of small biomolecule interactions using a plasmonic tilted fiber grating sensor. *Journal of Lightwave Technology*. 2019;**37**(11):2792-2799

[49] He YL et al. Fiber bragg grating monitoring of a morphing wing based on a polyvinyl chloride reinforced silicone substrate. *Optical Fiber Technology*. 2019;**50**:145-153

[50] Lao JJ et al. Gold nanoparticle-functionalized surface Plasmon resonance optical Fiber biosensor: In situ detection of thrombin with 1 n.M detection limit. *Journal of Lightwave Technology*. 2019;**37**(11):2748-2755

[51] Lobry M et al. Non-enzymatic D-glucose plasmonic optical fiber grating biosensor. *Biosensors & Bioelectronics*. 2019;**142**

- [52] Loyez M et al. Functionalized gold electroless-plated optical fiber gratings for reliable surface biosensing. *Sensors and Actuators B: Chemical*. 2019;**280**:54-61
- [53] Sypabekova M et al. Functionalized etched tilted fiber Bragg grating aptasensor for label-free protein detection. *Biosensors & Bioelectronics*. 2019;**146**
- [54] Fan XC et al. Target-induced autonomous synthesis of G-quadruplex sequences for label-free and amplified fluorescent aptasensing of mucin 1. *Sensors and Actuators B: Chemical*. 2020;**304**
- [55] Li J et al. Glucose assay based on a fluorescent multi-hydroxyl carbon dots reversible assembly with phenylboronic acid brush grafted magnetic nanoparticles. *Sensors and Actuators B: Chemical*. 2020;**304**
- [56] Raducanu VS et al. A direct fluorescent signal transducer embedded in a DNA aptamer paves the way for versatile metal-ion detection. *Sensors and Actuators B: Chemical*. 2020;**304**
- [57] Tang YY et al. A robust OFF-ON fluorescent biosensor for detection and clearance of bacterial endotoxin by specific peptide based aggregation induced emission. *Sensors and Actuators B: Chemical*. 2020;**304**
- [58] Zhang JY et al. F-containing initiator for ultrasensitive fluorescent detection of lung cancer DNA via atom transfer radical polymerization. *Analytica Chimica Acta*. 2020;**1094**:99-105
- [59] Yu J et al. Microfluidic paper-based chemiluminescence biosensor for simultaneous determination of glucose and uric acid. *Lab on a Chip*. 2011;**11**(7):1286-1291
- [60] Hu HL et al. Ni hierarchical structures supported on Titania nanowire arrays as efficient nonenzymatic glucose sensor. *Journal of Nanoscience and Nanotechnology*. 2020;**20**(5):3246-3251
- [61] Hui YY et al. An electrochemical aptasensor based on DNA-AuNPs-HRP nanoprobe and exonuclease-assisted signal amplification for detection of aflatoxin B-1. *Food Control*. 2020;**109**
- [62] Peyman H, Roshanfekr H, Ansari S. DNA-based electrochemical biosensor using chitosan-carbon nanotubes composite film for biodetection of Pirazon. *Eurasian Chemical Communication*. 2020;**2**(2):213-225
- [63] Sundar S, Kwon SJ, Venkatachalam G. Magneto-biosensor for the detection of uric acid using citric acid-capped Iron oxide nanoparticles. *Journal of Nanoscience and Nanotechnology*. 2020;**20**(4):2144-2153
- [64] Vathani AM et al. Fabrication of Al-TiO₂ thin film electrode by spray pyrolysis technique for urea sensing. *Journal of Nanoscience and Nanotechnology*. 2020;**20**(5):2887-2892
- [65] Fu QQ et al. Ambient light sensor based colorimetric dipstick reader for rapid monitoring organophosphate pesticides on a smart phone. *Analytica Chimica Acta*. 2019;**1092**:126-131
- [66] Huang LT, Li ZH, Guo LQ. Colorimetric assay of acetylcholinesterase inhibitor tacrine based on MoO₂ nanoparticles as peroxidase mimetics. *Spectrochimica Acta Part a-Molecular and Biomolecular Spectroscopy*. 2020;**224**
- [67] Jia M et al. Extended GR-5 DNAzyme-based autonomous isothermal Cascade machine: An efficient and sensitive

- one-tube colorimetric platform for Pb²⁺ detection. *Sensors and Actuators B: Chemical*. 2020;**304**
- [68] Kong LB et al. A novel smartphone-based CD-spectrometer for high sensitive and cost-effective colorimetric detection of ascorbic acid. *Analytica Chimica Acta*. 2020;**1093**:150-159
- [69] Wei SQ et al. Exponential amplification reaction and triplex DNA mediated aggregation of gold nanoparticles for sensitive colorimetric detection of microRNA. *Analytica Chimica Acta*. 2020;**1095**:179-184
- [70] Kim KI et al. Influence of temperature and humidity on the detection of benzene vapor by a piezoelectric crystal sensor. *Instrumentation Science & Technology*. 2019;**47**(4):436-447
- [71] Pohanka M. Piezoelectric Immunosensor for the determination of C-reactive protein. *International Journal of Electrochemical Science*. 2019;**14**(9):8470-8478
- [72] Urdinola KB et al. In-Silico Prediction on the MSAMS-Assisted Immobilization of Bovine Serum Albumin on 10 MHz Piezoelectric Immunosensors. *Journal of Molecular and Engineering Materials*. 2019;**7**(1-2)
- [73] Yuan M et al. Piezoelectric arsenite aptasensor based on the use of a self-assembled mercaptoethylamine monolayer and gold nanoparticles. *Microchimica Acta*. 2019;**186**(5)
- [74] Zamora-Sequeira R et al. What are the Main Sensor Methods for Quantifying Pesticides in Agricultural Activities? A Review. *Molecules*. 2019;**24**(14)
- [75] Katchman BA et al. Eccrine Sweat as a Biofluid for Profiling Immune Biomarkers. *Proteomics Clinical Applications*. 2018;**12**(6)
- [76] Adewole OO et al. Proteomic profiling of eccrine sweat reveals its potential as a diagnostic biofluid for active tuberculosis. *Proteomics Clinical Applications*. 2016;**10**(5):547-553
- [77] Hagan S, Martin E, Enriquez-de-Salamanca A. Tear fluid biomarkers in ocular and systemic disease: Potential use for predictive, preventive and personalised medicine. *Epma Journal*. 2016;**7**
- [78] Belstrøm D et al. Salivary cytokine levels in early gingival inflammation. *Journal of Oral Microbiology*. 2017;**9**(1)
- [79] Viswanath B et al. Recent trends in the development of diagnostic tools for diabetes mellitus using patient saliva. *Trends in Analytical Chemistry*. 2017;**89**:60-67
- [80] Sánchez-Tirado E et al. Magnetic multiwalled carbon nanotubes as nanocarrier tags for sensitive determination of fetuin in saliva. *Biosensors and Bioelectronics*. 2018;**113**:88-94
- [81] Ana C et al. Dental caries and bacterial load in saliva and dental biofilm of type 1 diabetics on continuous subcutaneous insulin infusion. *Journal of Applied Oral Science*. 2018;**26**
- [82] Yamaguchi M. Microfluidic line-free mass sensor based on an antibody-modified mechanical resonator. *Micromachines*. 2018;**9**(4):13
- [83] Sharma N et al. Dopamine levels in human tear fluid. *Indian Journal of Ophthalmology*. 2019;**67**(1):38-41
- [84] Hladek MD et al. Using sweat to measure cytokines in older adults compared to younger adults: A pilot study. *Journal of Immunological Methods*. 2018;**454**:1-5
- [85] Chandra P et al. Separation and simultaneous detection of anticancer

drugs in a microfluidic device with an amperometric biosensor. *Biosensors and Bioelectronics*. 2011;**28**(1):326-332

[86] Andrianova MS et al. CMOS-compatible biosensor for L-carnitine detection. *Biosensors and Bioelectronics*. 2018;**119**:48-54

[87] Soler M et al. Multiplexed nanoplasmonic biosensor for one-step simultaneous detection of chlamydia trachomatis and *Neisseria gonorrhoeae* in urine. *Biosensors and Bioelectronics*. 2017;**94**:560-567

[88] Myszka DG. Handbook of surface Plasmon resonance 2nd edition foreword to the 1st edition. In: Schasfoort RBM, editor. Handbook of surface Plasmon resonance, 2nd edition. 2017. pp. V-IX

[89] Zhu JY et al. An integrated adipose-tissue-on-chip nanoplasmonic biosensing platform for investigating obesity-associated inflammation. *Lab on a Chip*. 2018;**18**(23):3550-3560

[90] Vazquez-Guardado A et al. Enzyme-free plasmonic biosensor for direct detection of neurotransmitter dopamine from whole blood. *Nano Letters*. 2019;**19**(1):449-454

[91] Li XK et al. Label-Free Optofluidic Nanobiosensor Enables Real-Time Analysis of Single-Cell Cytokine Secretion. *Small*. 2018;**14**(26)

[92] Mi SL et al. An integrated microchannel biosensor platform to analyse low density lactate metabolism in HepG2 cells in vitro. *RSC Advances*. 2019;**9**(16):9006-9013

[93] Evans D et al. A novel microfluidic point-of-care biosensor system on printed circuit board for cytokine detection. *Sensors*. 2018;**18**(11)

[94] Garcia M, Alonso-Fernandez J, Escarpa A. Copper nanowires immobilized on the boards of

microfluidic chips for the rapid and simultaneous diagnosis of Galactosemia diseases in Newborn urine samples. *Analytical Chemistry*. 2013;**85**(19):9116-9125

[95] Oliveira MC et al. Nonenzymatic sensor for determination of glucose in blood plasma based on nickel oxyhydroxide in a microfluidic system of cotton thread. *Journal of Electroanalytical Chemistry*. 2019;**840**:153-159

[96] Chungchai W et al. Development of a novel three-dimensional microfluidic paper-based analytical device (3D- μ PAD) for chlorpyrifos detection using graphene quantum-dot capped gold nanocomposite for colorimetric assay. *International Journal of Environmental Analytical Chemistry*

[97] Fakhri N et al. Paper based colorimetric detection of miRNA-21 using Ag/Pt nanoclusters. *Spectrochimica Acta Part a-Molecular and Biomolecular Spectroscopy*. 2020;**227**

[98] Li F et al. High-resolution temporally resolved chemiluminescence based on double-layered 3D microfluidic paper-based device for multiplexed analysis. *Biosensors & Bioelectronics*. 2019;**141**

[99] Hossain SMZ, Brennan JD. Beta-Galactosidase-based colorimetric paper sensor for determination of heavy metals. *Analytical Chemistry*. 2011;**83**(22):8772-8778

[100] Lin Y et al. Detection of heavy metal by paper-based microfluidics. *Biosensors and Bioelectronics*. 2016;**83**:256-266

[101] Fraser LA et al. A portable microfluidic Aptamer-tethered enzyme capture (APTEC) biosensor for malaria diagnosis. *Biosensors and Bioelectronics*. 2018;**100**:591-596

Chapter

Biological Bone Micro Grinding Temperature Field under Nanoparticle Jet Mist Cooling

Min Yang, Changhe Li, Liang Luo, Lan Dong, Dongzhou Jia, Runze Li, Mingzheng Liu, Xin Cui, Yali Hou, Yanbin Zhang, Teng Gao, Xiaoming Wang and Yunze Long

Abstract

Clinical neurosurgeons used micro grinding to remove bone tissues, and drip irrigation-type normal saline (NS) is used with low cooling efficiency. Osteonecrosis and irreversible thermal neural injury caused by excessively high grinding temperature are bottleneck problems in neurosurgery and have severely restricted the application of micro grinding in surgical procedures. Therefore, a nanoparticle jet mist cooling (NJMC) bio-bone micro grinding process is put forward in this chapter. The nanofluid convective heat transfer mechanism in the micro grinding zone is investigated, and heat transfer enhancement mechanism of solid nanoparticles and heat distribution mechanism in the micro grinding zone are revealed. On this basis, a temperature field model of NJMC bio-bone micro grinding is established. An experimental platform of NJMC bio-bone micro grinding is constructed, and bone micro grinding force and temperatures at different measuring points on the bone surface are measured. The results indicated that the model error of temperature field is 6.7%, theoretical analysis basically accorded with experimental results, thus certifying the correctness of the dynamic temperature field in NJMC bio-bone micro grinding.

Keywords: grinding, nanoparticle jet, mist cooling, biological bone, thermal injury, temperature field

1. Introduction

As a precise material removal method, grinding has been extensively applied to bone tissue removal and surface treatment in surgical procedures by conforming to the combining trend of machine science and biomedical science. In the machining field, the method of using miniature grinding tools (diameter is generally below 1 mm) for machining of feature size of 1~500 μm is called micro grinding [1]. As bone tissues processed in osteological surgery are viable tissues and diamond grinding tool has obviously higher specific energy in the grinding process than other cutting methods, human bone, nerves, and blood vessels can be easily influenced by high temperature, and when grinding temperature is higher than 50°C, bone tissues

will experience irreversible necrosis, and nervous tissues will start experiencing thermal injury at 43°C [2]. In the present neurosurgery, surgeons usually perform drip irrigation of normal saline (NS) in the grinding zone following the following principle: The heat is carried away through convective heat transfer so as to cool the operative region. However, the drip irrigation-type cooling efficiency is not ideal; thermal injury in the operation process leads to necrosis of surrounding tissues and nerves, so the operation fails. The irreversible thermal injury of bone tissues triggered by high temperature in micro grinding is a bottleneck problem in bone micro grinding operation. Moreover, a large quantity of cooling liquid needs to be dripped into the grinding zone under drip irrigation-type cooling, which can easily reduce the visibility of the operative region under an endoscope [3].

In the machining field, as flood cooling grinding harms worker's health and the environment, dry grinding can easily result in serious burn of the specimen, and microdroplet jet grinding has insufficient cooling performance [4–7]; researchers have put forward nanoparticle jet mist cooling (NJMC) technique according to the theory of heat transfer enhancement, which cannot only enhance the convective heat transfer in the grinding zone by taking full advantages of high specific surface of nanoparticles and heat capacity but, meanwhile, can improve the tribological properties of the grinding zone and can reduce heat generation by virtue of superior antifriction and anti-wear characteristics and high bearing capacity of nanoparticles [8–10]. On this basis, as it is the fact that clinical surgical bone grinding has disadvantages of thermal injury and low visibility of operative region and that nanofluid microdroplet grinding has good cooling and lubrication effect with a small use level of cutting fluid in the machining field, the research team where the author joined proposed NJMC bio-bone micro grinding process: adding medical solid nanoparticles of a certain proportion into the NS and selecting the corresponding surface dispersant according to physical and chemical properties of nanoparticle material, supplemented by ultrasonic vibration, so medical nanoparticles can enjoy uniform and stable distribution in the NS so as to form a medical nanofluid under stable suspension, which is then sprayed into the focus grinding zone in jet form as carried by high-pressure gas via a miniature nozzle [11, 12]. And this is expected to lower the bone grinding temperature while improving the visibility of the operative region.

In recent years, researches have initially explored into thermal injury problem existing in the bio-bone grinding process. Taking heat transfer problem and its inverse problem in the bone grinding process with a miniature spherical grinding tool, Zhang et al. [13] conducted an in-depth study combining numerical simulation and experiment and analyzed the transient temperature field in the bone grinding process through a numerical simulation based on a heat generation model of bone grinding. Directing at the complex structure of bone issues and taking grinding temperature, grinding force, and blocking of grinding tool in the bone tissue grinding process as the study objects, Zhu et al. [14] obtained the grinding tool blocking mechanism in the bone tissue grinding by analyzing action rules of grinding temperatures on grinding temperature, grinding force, and grinding tool blocking. Sasaki et al. [15] analyzed heat generation during grinding using diamond tools with a diameter of 5 mm at a rotational speed of 100,000 r/min. They found that grinding for 10 cm along the grinding temperature without cooling liquid will expand the area of higher than 37.7°C continuously. To prevent thermal injuries to surrounding nerve tissues, Enomoto et al. [16] invented a new diamond spherical tool that can effectively reduce the temperature at the grinding zone. The surface of the diamond tool contains adsorbed super-hydrophilic TiO₂ nanoparticles, which effectively prevent temperature rise during bone grinding. The grinding zone is cooled during neurosurgery commonly by dripping a room-temperature NS into it.

The NS dissipates heat through natural heat convection, cooling the high-temperature region.

For the bottleneck problem in the current clinical neurosurgical bone operation, namely irreversible thermal injury, a NJMC bio-bone micro grinding process was put forward. The convective heat transfer mechanism of nanofluid in micro grinding zone was studied. A dynamic temperature field model in NJMC bio-bone grinding was constructed. By reference to the suppression measures of grinding thermal injury in the field of mechanical engineering, the bottleneck in orthopedic operation was solved so as to provide theoretical guidance and technical support for avoiding or reducing thermal injury in clinical orthopedic operation.

2. Grinding temperature field

Starting from the universal temperature field problem, the heat quantity Q at one spatial point takes place transiently, and the temperatures at other points nearby this point will be changed under the action of the transferred heat quantity, and meanwhile, they are variable due to the spatial-temporal change. Temperature field is a generic term of temperature distribution at spatial points at a certain time. Generally speaking, temperature field is a function of space and time [17]:

$$T = f(x, y, z, t) \quad (1)$$

Equation (1) denotes a three-dimensional (3D) unsteady-state temperature field where the object temperature is changed both in direction x , y , and z and at time t . In this study, temperature field is divided into two types:

1. It is divided into steady-state temperature field and transient-state temperature field according to whether temperature changes with time. As indicated by Eq. (1), if the temperature field does not change with time, namely $\frac{\partial T}{\partial t} = 0$, it is a steady-state temperature field, or otherwise it is a transient-state temperature field. As mobile heat source is loaded, the temperature at specific point on the bone surface presents time-dependent change. Hence, the temperature field studied in this chapter is transient-state temperature field.
2. It is divided into temperature field in cut-in zone, that in steady-state zone and that in cut-out zone according to the grinding tool/specimen contact arc length. As shown in **Figure 1**, the effective cutting part of the grinding tool is totally within the length of the specimen material, the grinding tool/specimen contact arc length is l_c , and the temperature field is temperature field in steady-state zone. As the grinding process starts, the grinding tool/specimen

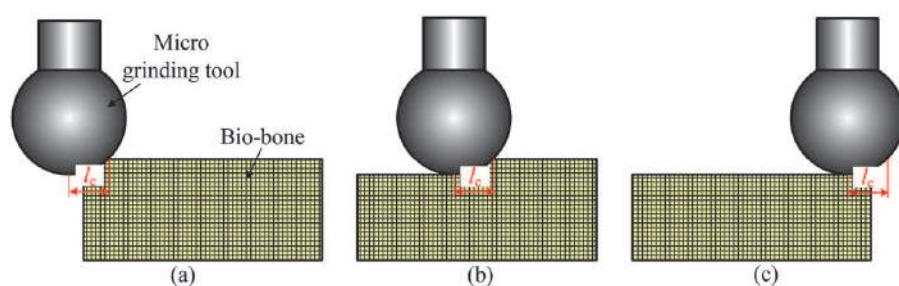


Figure 1. Schematic diagram of abrasive/bone contact states. (a) Cut-in zone. (b) Steady-state zone. (c) Cut-out zone.

contact arc length is gradually enlarged, but not reaching l_c , and at the moment, the grinding tool/specimen material is in cut-in phase, so the temperature field is in cut-in zone. As the grinding tool starts moving out of the specimen length, the contact arc length is gradually reduced to 0, and at the time, the grinding tool cuts out the specimen material, so the temperature is in cut-out zone.

2.1 The solution method of grinding temperature field

The solving method of grinding temperature field includes analytical method and finite difference method.

2.1.1 Solution of grinding temperature field by analytical method

Following the heat transfer theory and energy conservation law, analytical method solves the temperature rise function based on all kinds of boundary conditions in actual grinding machining so as to obtain temperature values on specimen surface and each internal node. The advantage of the analytical method is that it cannot only obtain the functional relationship regarding temperature distribution but also analyze different influence factors related to temperature field and their influence laws on temperature field distribution. Based on the theory of mobile heat source proposed by Jaeger [18] in 1942, many researchers have established theoretical grinding heat models with the main idea being superposition method of heat source temperature field. In other words, grinding interface is regarded as surface heat source constituted by numerous linear heat sources while linear heat sources are treated as a combination of numerous tiny unit linear heat sources, and each tiny unit linear heat source is simplified into combined action of point heat sources. Therefore, the basis for superposition method of heat source temperature fields is the solution of this temperature field at any time after transient point heat sources in an infinite object instantaneously emit partial heat quantity.

2.1.2 Solution of grinding temperature field by finite difference method

As for solving the grinding temperature field, it can be complicated to use analytical method to solve even simple heat conduction problem. Grinding machining is itself of high complexity relative to other machining modes [19, 20], where input parameters of grinding temperature field are miscellaneous, abrasive particle distribution is irregular, grinding state of abrasive particle (plowing, sliding, cutting) is uncertain, cooling medium participates in convective heat transfer in the grinding zone, and surrounding airflow field of grinding tool has an effect on temperature. A large quantity of nonlinear coupling relations exists in the grinding process, so if any input parameter is changed, it will influence the follow-up derivation of expressions, and the solving of temperature field becomes even harder for the analytical method [21, 22]. Under this circumstance, the finite element method based on numerical method is a very effective method of solving heat conduction problem. It is only necessary to determine boundary conditions and initial conditions in order to conveniently calculate grinding temperature field, so it has been widely used by researchers at present. As the finite element method makes many hypotheses for grinding temperature field and boundary conditions, only specific built-in modules of specific software can be used [23], and the deviation of calculated grinding temperature from actual temperature is large. The finite element method based on numerical method is another effective method of calculating grinding temperature field between analytical method and finite element method.

It can accurately calculate temperature field through a theoretical modeling of boundary conditions of temperature field (heat flux, heat distribution ratio, convective heat transfer coefficient, etc.) according to actual grinding conditions. There have been few reports on calculation of grinding temperature field via finite difference method, so this method will be hereby described in details.

2.1.2.1 Basic principle of finite difference method

The object is divided into finite grid cells. A difference equation is obtained by transforming the differential equation, and the temperature at each grid cell node is solved through numerical simulation. As shown in **Figure 2**, under the 2D heat conduction problem, the object is divided into rectangular grids along directions x and y according to the spacing between Δx and Δy . The node is defined as intersection point of each grid line, $p(i, j)$ denotes the position of each node, i is serial number at node along the direction x , j is serial number at node along the direction y , and the intersection point between object boundary and grid is defined as boundary node. The basic principle of this method is to replace differential quotient with finite difference quotient so as to transform the original differential equation into a difference Equation [24].

2.1.2.2 Establishment of differential equation of heat conduction

In the grinding heat conduction problem, Fourier's law is the most fundamental heat conduction equation, namely the heat quantity passing through infinitesimal isothermal surface A within limited time interval t is Q , which is in direct proportion of temperature gradient $\frac{\partial T}{\partial n}$ and is contrary to the direction of temperature field:

$$dQ = -k_w \frac{\partial T}{\partial n} dA dt \quad (2)$$

For heat flux:

$$q_x = -k_w \frac{\partial T}{\partial x} \quad (3)$$

where q_x is heat flux in direction x and $\frac{\partial T}{\partial x}$ is temperature field in direction x .

The differential equation of heat conduction can be obtained according to Fourier's law and energy conservation law, and it is hypothesized that there is internal heat source in the object. Based on the above hypothesis, microelement

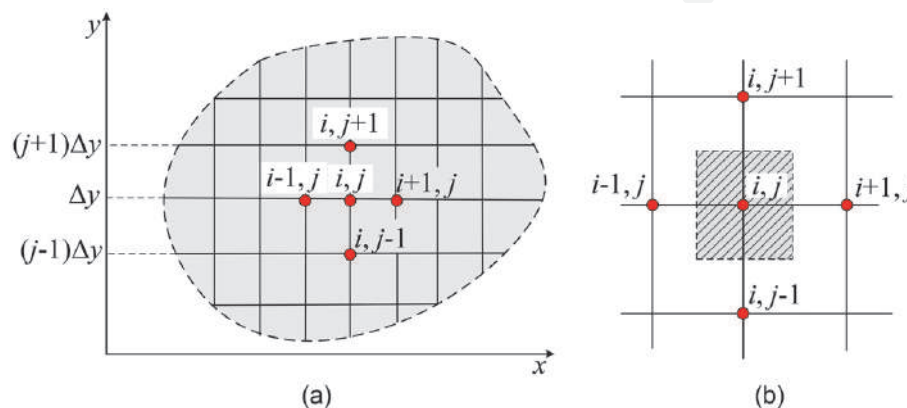


Figure 2. Schematic diagram of gridlines and nodes of finite difference method. (a) Grid element. (b) Grid node.

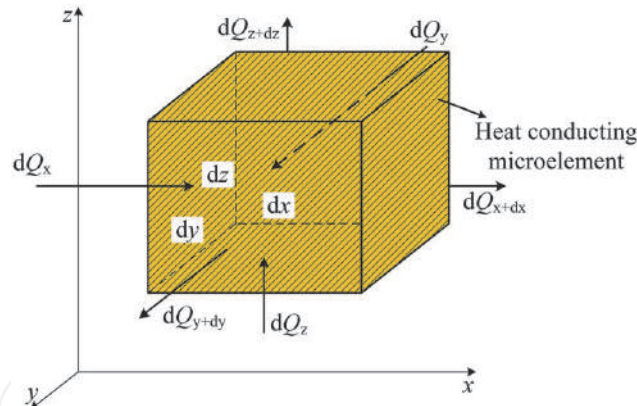


Figure 3.
Schematic diagram of thermal conductive microelement.

$dV = dx$ is divided from the object under heat conduction. As shown in **Figure 3**, the three edges of this microelement are parallel to axes x , y , and z , respectively. Thermal equilibrium analysis of the microelement is conducted. It can be known from the energy conservation law that the net heat quantity transferred in and out of the microelement within time dt should be equal to increment of internal energy in the microelement, namely net heat quantity transferred in and out of the microelement (I) and increment of internal energy in the microelement (II).

Net heat quantity transferred in and out of the microelement and increment of internal energy in the microelement will be, respectively, calculated as follows.

Energy equilibrium analysis is implemented for the microelement in **Figure 3**. The net quantity transferred in and out of the microelement can be obtained by adding the net heat quantities transferred in and out of the microelement from directions x , y , and z , respectively. Along the direction of axis x , the heat quantity transferred in the microelement within time dt through plane x is:

$$dQ_x = q_x dydzdt \quad (4)$$

The heat quantity transferred out through plane $x + dx$:

$$dQ_{x+dx} = q_{x+dx} dydzdt \quad (5)$$

where $q_{x+dx} = q_x + \frac{\partial q_x}{\partial x} dx$.

Hence, the net heat quantity transferred in and out of the microelement along the direction of axis x within time dt is:

$$dQ_x - dQ_{x+dx} = -\frac{\partial q_x}{\partial x} dx dy dz dt \quad (6)$$

Similarly, the net quantities transferred in and out of the microelement along the directions of axes y and z within this time are, respectively:

$$dQ_y - dQ_{y+dy} = -\frac{\partial q_y}{\partial y} dx dy dz dt \quad (7)$$

$$dQ_z - dQ_{z+dz} = -\frac{\partial q_z}{\partial z} dx dy dz dt \quad (8)$$

The following is obtained by adding net quantities transferred in and out of the microelement in directions x , y , and z :

$$I = -\left(\frac{\partial q_x}{\partial x} + \frac{\partial q_y}{\partial y} + \frac{\partial q_z}{\partial z}\right) dx dy dz dt \quad (9)$$

Within time dt , the increment of internal energy in the microelement is:

$$II = \rho c \frac{\partial T}{\partial t} dx dy dz dt \quad (10)$$

where ρ is density of point heat source heat conducting medium and c is the specific heat.

The three-dimensional heat conduction model can be obtained by Eqs. (9) and (10):

$$\frac{\partial T}{\partial t} = \alpha_t \left(\frac{\partial^2 T}{\partial x^2} + \frac{\partial^2 T}{\partial y^2} + \frac{\partial^2 T}{\partial z^2} \right) \quad (11)$$

where α_t is thermal diffusion coefficient of point heat source heat conducting medium.

2.1.2.3 Differential equation converted into difference equation

This specimen is assumed as a rectangular plane, and it is discretely decomposed into a planar grid structure. Isometric spatial step length $\Delta x = \Delta z = \Delta l$ is taken; two groups of equally spaced parallel lines are drawn to subdivide the rectangular specimen and the equation of parallel line:

$$\begin{cases} x = x_i = i\Delta l, i = 0, 1, \dots, M, M\Delta l = l_w \\ z = z_j = j\Delta l, j = 0, 1, \dots, N, N\Delta l = b_w \end{cases} \quad (12)$$

where x_i and z_j are coordinate value of transverse line i in direction x and coordinate value of vertical line j in direction z , respectively, and both lines constitute the difference grid; l_w and b_w are specimen length and height, respectively; and M and N are natural numbers.

The grid area of difference calculation is obtained through subdivision as shown in **Figure 3**.

A set of difference equations is built based on second-order difference quotient, namely:

$$\begin{cases} \frac{\partial^2 T}{\partial x^2}(i, j) = \frac{T(i+1, j) + T(i-1, j) - 2T(i, j)}{\Delta l^2} + O(\Delta l^2) \\ \frac{\partial^2 T}{\partial z^2}(i, j) = \frac{T(i, j+1) + T(i, j-1) - 2T(i, j)}{\Delta l^2} + O(\Delta l^2) \\ \frac{\partial T}{\partial t}(i, j) = \frac{T_{t+\Delta t}(i, j) - T_t(i, j)}{\Delta t} + O(\Delta t) \end{cases} \quad (13)$$

The difference equation of each node in the grid can be obtained:

$$\begin{aligned} T_{t+\Delta t}(i, j) = & \frac{\Delta t \{ k_x \cdot [T(i, j+1) + T(i, j-1)] + k_z \cdot [T(i+1, j) + T(i-1, j)] \}}{\rho_w c_w \Delta l^2} \\ & + \left[1 - \frac{2\Delta t(k_x + k_z)}{\rho_w c_w \Delta l^2} \right] T_t(i, j) \end{aligned} \quad (14)$$

2.2 Boundary condition

Heat transfer means transferring heat quantity from a system to another system with three main forms: convection, heat conduction, and radiation [25, 26]. The grinding tool/specimen contact interface is cooled with grinding fluid in the grinding process, so the grinding fluid flowing at this interface will conduct heat transfer on the specimen surface, where the main heat transfer form is convective heat transfer. As the grinding fluid contacts the specimen surface, partial heat quantity on the specimen surface is brought away by cooling fluid via convective heat transfer, and the residual heat stays on the specimen matrix and is transferred inside it. Therefore, the cooling effect of the machining zone can be strengthened by cooling fluid or by enhancing its heat transfer performance [27]. The temperature of external medium and convective heat transfer coefficient on boundary are given as shown in **Figure 4**. The heat quantity at grinding interface is generated due to grinding action of grinding tool and brought away by external cooling medium. In the meantime, both cooling medium and adjacent node $(i-1, 1)$ on the specimen surface contact this node $(i, 1)$, so the heat quantity at this node will be transferred to cooling medium in convective way and also to adjacent node, and in the end, a stable temperature is reached at grinding tool/specimen interface [28].

The thermal equilibrium analysis of heat conduction in temperature field is to solve differential equation. The complete description of heat conduction process includes monodromy conditions and differential equation of heat conduction, where the former includes time condition, physical condition, geometrical condition, and boundary condition [29]. The boundary condition specifies characteristics of heat transfer process on object boundary, namely reflecting conditions for interaction between heat transfer process and surroundings, so initial condition (temperature at $t = 0$) and boundary conditions (set temperature in boundary region or input and output heat fluxes) must be set in the temperature field. Based on the heat transfer theory, thermodynamic boundary conditions are generally divided into the three following types [30].

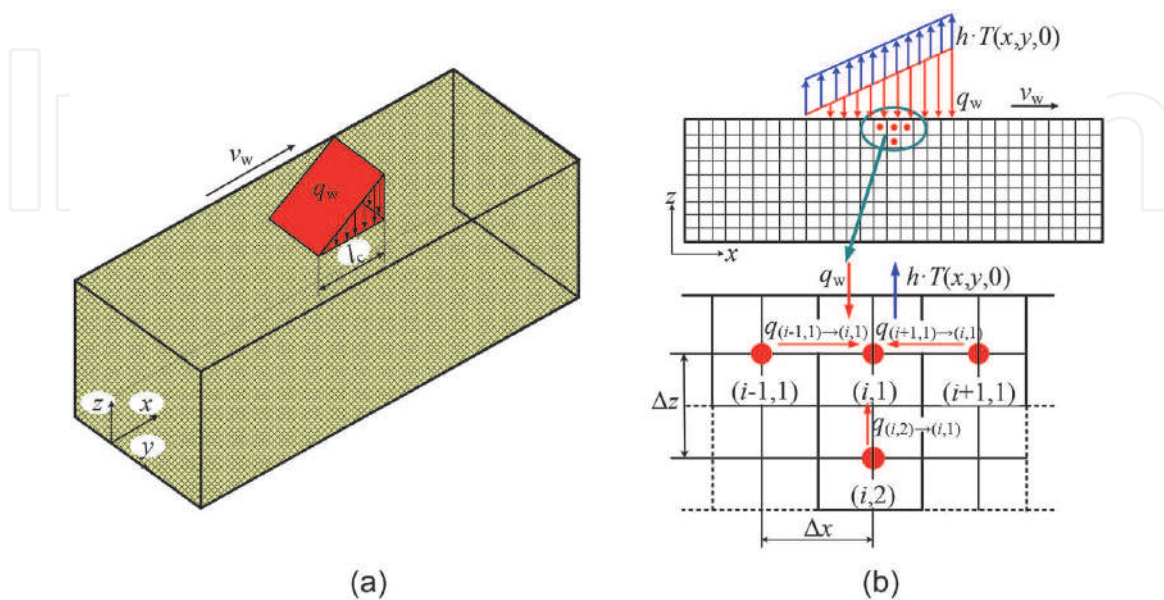


Figure 4. Schematic diagram of heat conduction model and convective heat transfer at grinding interface. (a) Heat conduction model. (b) Convective heat transfer at grinding interface.

2.2.1 The first kind of boundary conditions

Boundary condition of this type is forced convective boundary condition, namely temperature value at boundary of the given object at any time, and it is also called Dirichlet condition:

$$T|_{s_f} = T_w \quad (15)$$

where T_w is set temperature at boundary surface s_f . If boundary temperature is kept unchanged, T_w is a fixed value. If boundary temperature changes with time, T is a time-related functional expression.

2.2.2 The second kind of boundary conditions

Boundary condition of this type refers to heat flux on object boundary surface in normal direction at any time, and it is also called Neumann condition. The relationship between temperature gradient and heat flux is obtained through Fourier's law, and this is equivalent to temperature change rate on boundary s_f in normal direction at any time:

$$\left. \frac{\partial T}{\partial n} \right|_{s_f} = \frac{Q_w}{k} \quad (16)$$

where Q_w is heat quantity passing through boundary surface s_f . $Q_w = 0$ when the boundary is under thermal insulation. Q_w is a fixed value when heat conduction at the boundary is constant, and it is a time-related function when the heat conduction changes with time.

Differential equation at the second type of boundary:

$$\frac{\partial}{\partial x} \left(k_x \cdot \frac{\partial T}{\partial x} \right) + \frac{\partial}{\partial y} \left(k_y \cdot \frac{\partial T}{\partial y} \right) + \frac{\partial}{\partial z} \left(k_z \cdot \frac{\partial T}{\partial z} \right) = Q_w \quad (17)$$

2.2.3 The third kind of boundary conditions

Boundary condition of this type denotes convective heat transfer between boundary surface and surrounding medium, and it is also called Robin condition. It can be known from Newton's law of cooling that convective heat transfer occurs between boundary layer of the specimen and cooling heat transfer medium:

$$h(T|_{z=0} - T_0) - k \left. \frac{\partial T}{\partial z} \right|_{z=0} = q_w \quad (18)$$

where q_w is convective heat flux at the boundary surface s_f between cooling heat transfer medium and specimen and h is convective heat transfer coefficient at the boundary between cooling heat transfer medium and specimen.

Differential equation at the third type of boundary:

$$\frac{\partial}{\partial x} \left(k_x \cdot \frac{\partial T}{\partial x} \right) + \frac{\partial}{\partial y} \left(k_y \cdot \frac{\partial T}{\partial y} \right) + \frac{\partial}{\partial z} \left(k_z \cdot \frac{\partial T}{\partial z} \right) = h(T|_{s_f} - T_f) \quad (19)$$

2.3 Heat distribution coefficients

An important problem exists in the establishment process of temperature field model in the grinding zone. It is necessary to determine the proportion of grinding heat quantity transferred into the specimen, namely heat distribution coefficient R_w . Under non-dry grinding condition as shown in **Figure 4**, the total heat quantity generated in the grinding zone is [31]:

$$q_{\text{total}} = \frac{F_t v_s}{b_g l_c} = q_w + q_g + q_c + q_f \quad (20)$$

where b_g is width of grinding tool; q_w is heat quantity staying on the specimen surface; q_g is heat quantity transferred into abrasive particle of grinding tool; q_c is heat quantity carried away by grinding chips; and q_f is heat quantity transferred out by cooling medium.

The heat distribution coefficient model proposed by Rowe in consideration of convective heat transfer in the grinding zone is generally applied. As indicated by the model, under high-efficiency deep grinding, total energy in the grinding zone is transferred into grinding tool, grinding chips, grinding fluid, and theoretical mathematical model of specimen material, and furthermore, its feasibility has been proved by a large quantity of experimental results.

Heat flux transferred into specimen, grinding tool, grinding fluid, and grinding chips is correlated with parameters like maximum contact temperature T_{max} , boiling point T_b of grinding fluid, and melting point T_m of specimen ($T_{\text{max}} \leq T_b$) as shown in the following formula [32]:

$$\begin{cases} q_w = h_w \cdot T_{\text{max}} \\ q_g = h_g \cdot T_{\text{max}} \\ q_f = h_f \cdot T_{\text{max}} \\ q_c = h_d \cdot T_m \end{cases} \quad (21)$$

where h_w , h_g , h_f , and h_d are heat transfer coefficients of specimen material, grinding tool, grinding fluid, and grinding chips, respectively.

The proportion of heat quantity flowing into the specimen can be obtained as follows:

$$R_w = h_w \cdot T_{\text{max}} / q_{\text{total}} \quad (22)$$

3. Experimental study on micro grinding of biological bone with nanoparticle jet mist cooling

3.1 Nanoparticle jet mist cooling bone micro grinding experimental platform

Figure 5 shows the established experimental platform of NJMC bio-bone micro grinding, including feed system, fixed system, cooling system, and measuring system. Both axes x and y of the 3D displacement device are Shinano stepper motors, and axis z is Panasonic servo braking motor. A 120# diamond grinding tool is used, where the diameter of grinding head is 1 mm. The mist cooling supply device is mist

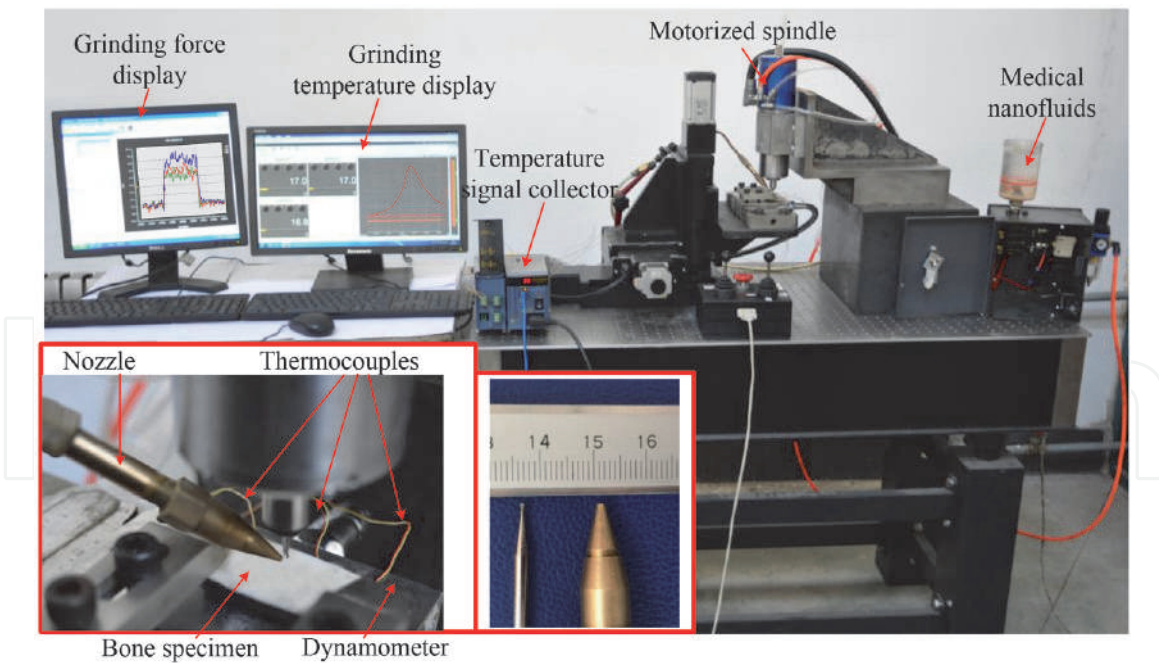


Figure 5.
 Nanoparticle jet mist cooling bone micro grinding experimental platform.

cooling supply system produced by Shanghai KINS Energy-Saving Technology Co., Ltd. The jet parameters are uniformly set in the experiment as shown in **Table 1**.

The clamping mode of thermocouple: a blind hole drilled on the back face of the bone specimen has a certain distance from the bone surface (grinding depth), the thermocouple wire is placed into the blind hole, the bone specimen is fixed on the dynamometer, and the force and temperature in the micro bone grinding process are simultaneously measured. Thermocouple type is K (TT-K-30), and measuring frequencies of both dynamometer and thermocouple are 100 Hz.

In the biomedical field, HA, SiO₂, and Al₂O₃ nanoparticles feature nontoxicity and good biological compatibility and are commonly used drug carriers in nanodrug release system [33, 34]; NS is a common clinically used cooling medium as osmotic pressure is basically equal to osmotic pressure of human plasma. Therefore, HA, SiO₂, and Al₂O₃ nanoparticles with a diameter of 50 nm were used as solid nanoscale additives and NS as a nanofluid base to prepare HA, SiO₂, and Al₂O₃ nanofluids. Polyethylene glycol 400 has been extensively applied to lubrication in colonoscopy and gastroscopy by virtue of superior lubricating property and nontoxicity, and its safety in human body has been clinically certified. In the meantime, PEG400 also has good dispersity. Therefore, PEG400 was used as dispersing agent in this

Jet parameters	Value
Nozzle diameter	$d_0 = 1 \text{ mm}$
Compressed gas pressure	$\Delta p = 0.5 \text{ MPa}$
Feed flow rate	$Q_f = 50 \text{ mL/h}$
Spray inclination angle	$\beta = 15^\circ$
Nozzle height	$H = 0.6 \text{ mm}$
Spray cone angle	$\alpha = 27^\circ$

Table 1.
 Table of mist cooling jet parameters.

chapter. When the dispersing agent with volume fraction of 2 vol.% and 2 vol.% is used, the suspension stability of the nanofluid will be the best. Hence, the nanofluid preparation method in this chapter was “two-step method,” namely adding 2 mL of HA, SiO₂, and Al₂O₃ nanoparticles and 0.2 mL of PE in 100 mL of NS supplemented with ultrasonic vibration for 15 min.

3.2 Temperature field of bio-bone micro grinding with different cooling methods

The dynamic temperature field model of NJMC bone grinding was verified. Different cooling modes were adopted: dry grinding, mist, and NJMC. As dynamic heat flux was loaded to theoretically calculate grinding temperature field, temperatures at different measuring points on the surface of the bone material were measured. As shown in **Figure 6**, three groups of thermocouples were used to simultaneously measure the temperatures at three measuring points—T1, T2, and T3—with spacing of 5 mm.

Figure 7(a) shows typical grinding force signals measured under dry grinding condition, where F_y is the force used to generate heat quantity.

The temperature field of bone micro grinding is solved under initial condition (room temperature) of $T_0 = 20^\circ\text{C}$. **Figure 8(a)** shows temperature curves measured at different measuring points under dry grinding condition and theoretical temperature curves. It can be known that in the bone grinding temperature curves, the peak values at three measuring points are 36.1°C , 38.2°C , and 36°C , respectively, and measured peak values at the three measuring points are 36.7°C , 38.5°C , and 36.6°C , respectively, namely the temperature on bone surface is ever-changing.

Figure 8(b) and **(c)** show peak values measured through the experiment at three measuring points under mist and NJMC conditions and those obtained through calculation. It can be known that in comparison with average temperature (36.8°C) on bone surface under dry grinding condition, the temperatures on the bone surface under mist and NJMC decline by 13.6% and 33.9%, respectively, thus proving the superior cooling effect of NJMC mode. The temperature error is 6.7%, and theoretical analysis basically accords with experimental result, which verifies the correctness of the dynamic temperature field in NJMC bio-bone micro grinding [35].

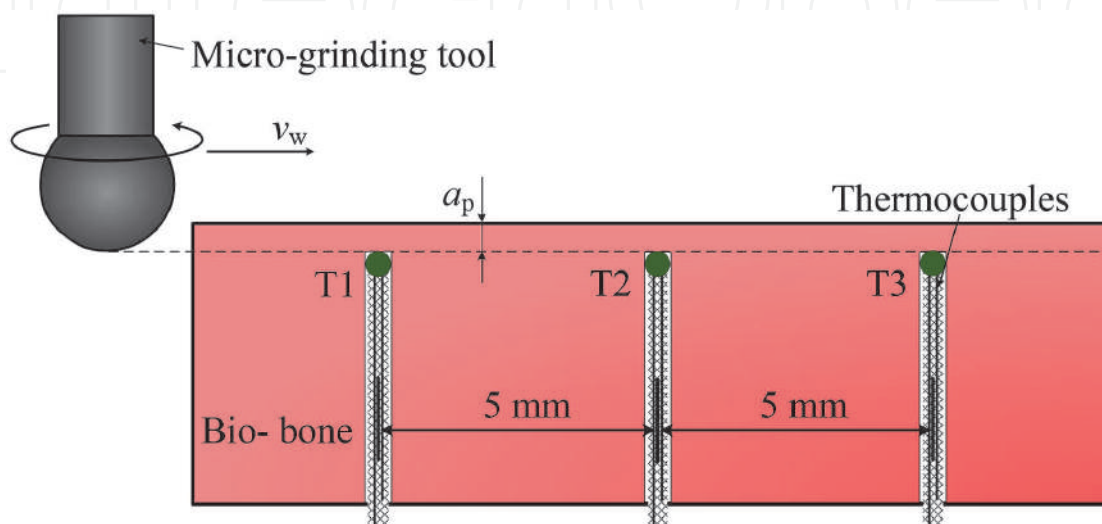


Figure 6. Schematic diagram of thermocouple clamping at different measuring points on bone surface.

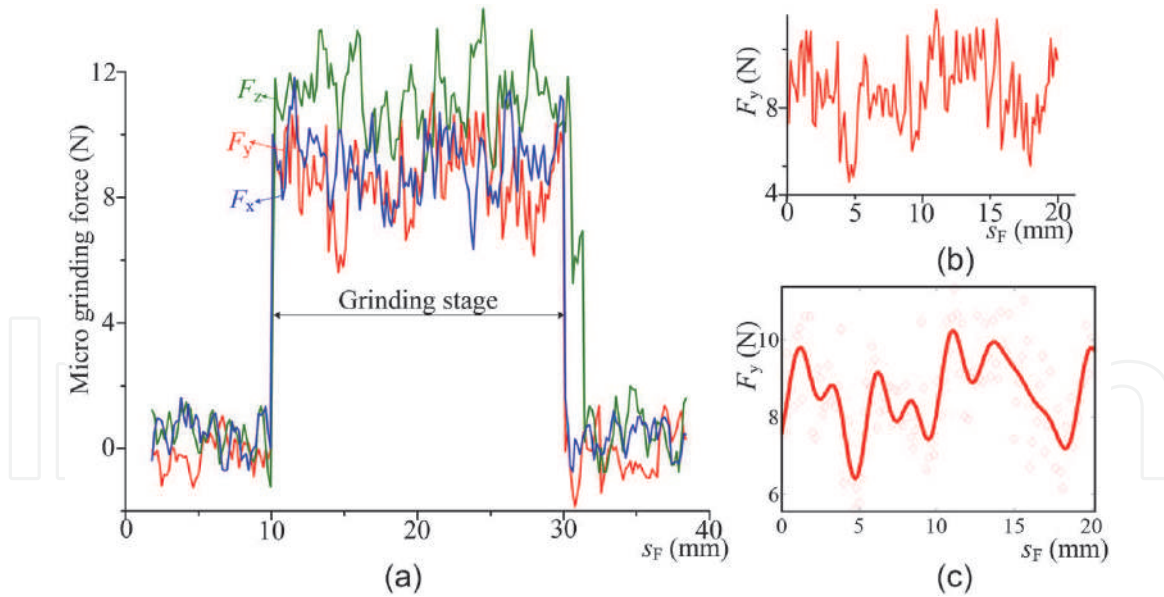


Figure 7. Typical force signals in micro grinding of biological bone materials. (a) Typical force signal of bio-bone micro grinding. (b) Grinding force in y direction. (c) Fitting curve of grinding force in y direction.

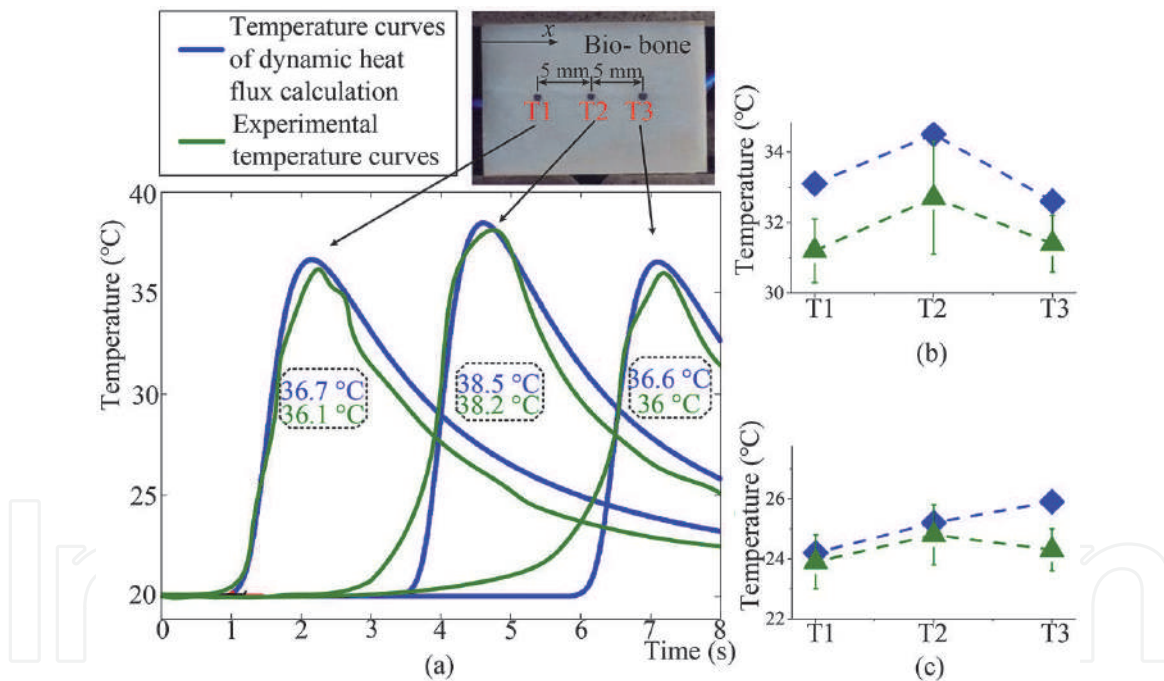


Figure 8. Temperature curves and values of different measuring points on bone surface under different cooling conditions. (a) Dry grinding temperature. (b) Mist cooling grinding temperature. (c) NJMC grinding temperature.

In order to explore into the dynamic characteristics of temperature field in bio-bone micro grinding, temperature fields in cut-in zone, steady-state zone, and cut-out zone are, respectively, analyzed. **Figures 9** and **10** show temperature fields and temperature curves in bone grinding under NJMC conditions. The detailed analysis process is as follows:

1. Cut-in zone: As shown in **Figures 9(a)** and **10**, as the grinding starts, the grinding tool starts contacting the material and gradually cuts into the material, undeformed cutting thickness is gradually increasing [36, 37], and the heat quantity generated at grinding interface starts migrating into the

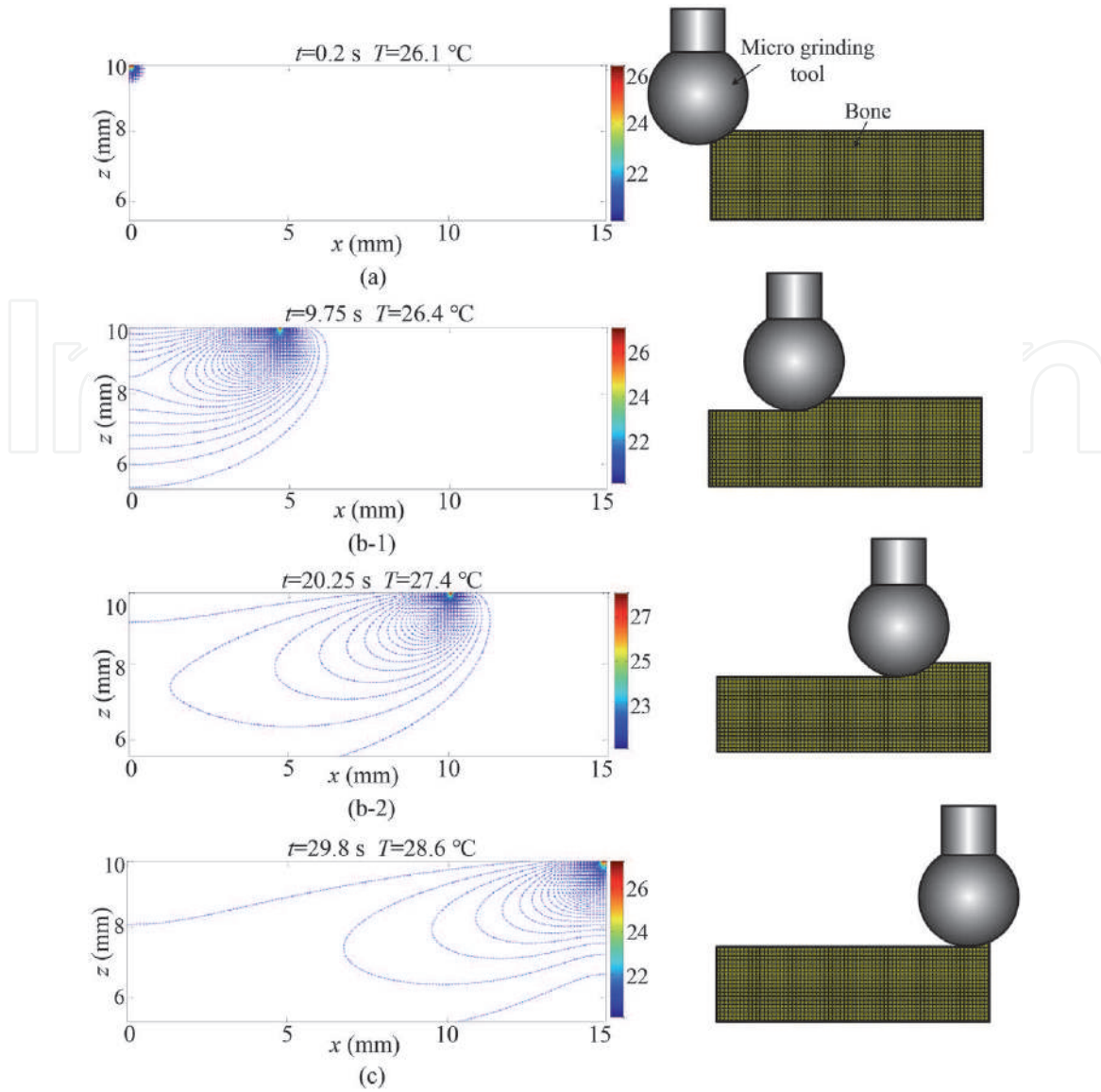


Figure 9. Temperature field in cut-in, steady-state, and cut-out zones of bone micro grinding. (a) Cut-in temperature field. (b-1) Steady-state temperature field. (b-2) Steady-state temperature field. (c) Cut-out temperature field.

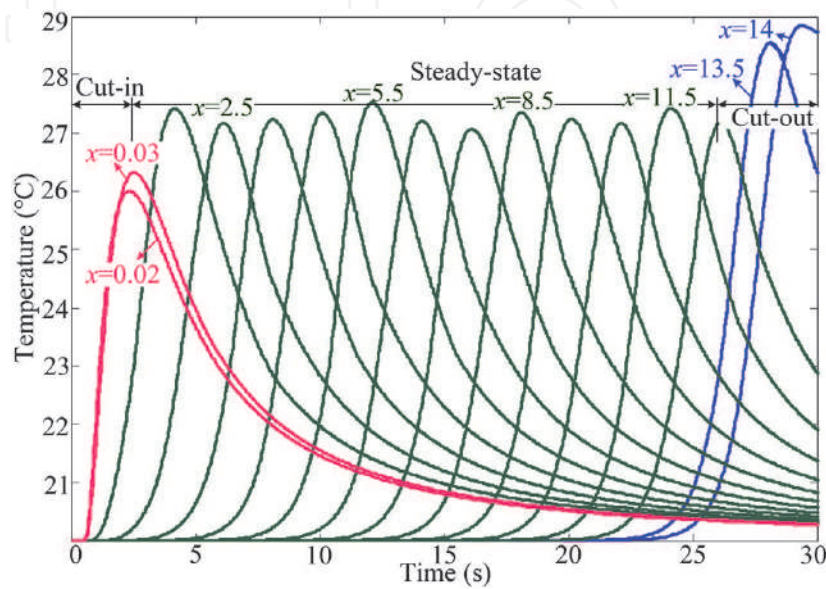


Figure 10. Temperature curves of cut-in, steady-state, and cut-out zones in bone micro grinding.

specimen surface. The temperature is low in the grinding zone, because the volume of material participating in the grinding in the cut-in zone is small with a small energy consumption.

2. Steady-state zone: In **Figures 9(b), (c)** and **10**, undeformed cutting thickness is kept at average value, and surface temperature no longer continues to rise, namely the formed temperature field reaches a steady state. As for grinding temperature fields calculated by researchers previously, after constant heat flux is loaded, the temperature value under which a steady state is reached will not be changed. However, in the temperature field of bone micro grinding with loaded dynamic heat flux as shown in the figure, the temperature value is ever-changing after the steady state is reached [38, 39].

3. Cut-out zone: As shown in **Figures 9(d)** and **10**, according to the heat transfer theory, undeformed thickness is gradually reduced when the grinding tool is in cut-out zone, and the volume of specimen material participating in the grinding action is continuously reduced. If the heat quantity generated at grinding interface remains unchanged, the volume of the material to which heat is migrated in the cut-out zone is continuously reduced. As heat conductivity coefficient of air is extremely low, more heat is aggregated in the grinding zone, and then grinding temperature rises to a great extent.

3.3 Effect of nanoparticle size on bone micro grinding temperature

To probe into the influence laws of nanoparticle size on bone micro grinding temperature, Al_2O_3 nanoparticles with particle sizes of 30, 50, 70, and 90 nm and NS were used to prepare nanofluids for bone grinding experiment and measure grinding force and temperature at measuring point T2 on the bone surface.

Figure 11(a) shows theoretical temperature curves under different cooling conditions, where abscissa axis denotes dimensionless distance ($x/l = 2v_w t/l_c$, $2l = l_c$), namely the location of this point in the grinding arc zone [40, 41]. It can be known from the figure that at the entry end in the contact zone, grinding temperature abruptly increases, peak temperature deviates from central position of heat source on the curve and deflects toward exit end of the contact zone, and the temperature at the exit end in the contact zone declines slowly. **Figure 11(b)** shows bone grinding temperatures measured using nanoparticles with different particle sizes, and it can be known that the grinding temperature increases with nanoparticle size.

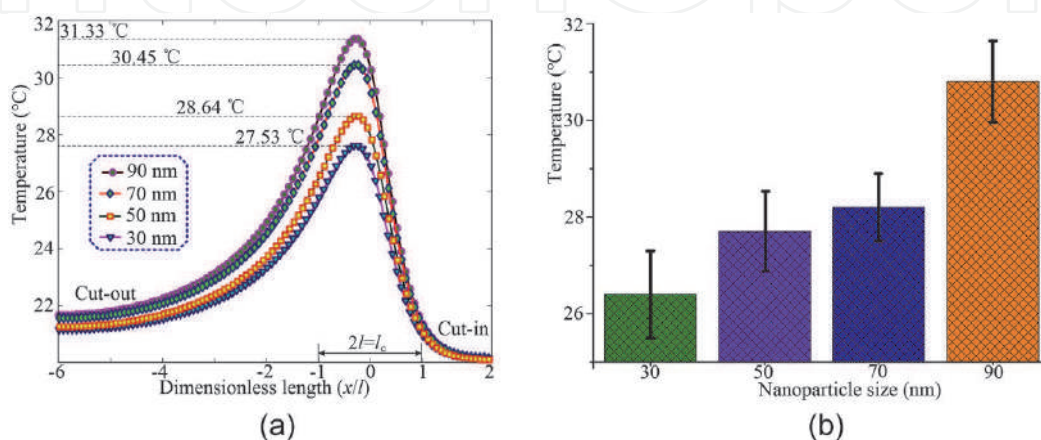


Figure 11. Micro grinding temperature with different nanoparticle size. (a) Theoretical calculated temperature value (b) theoretical calculated temperature value.

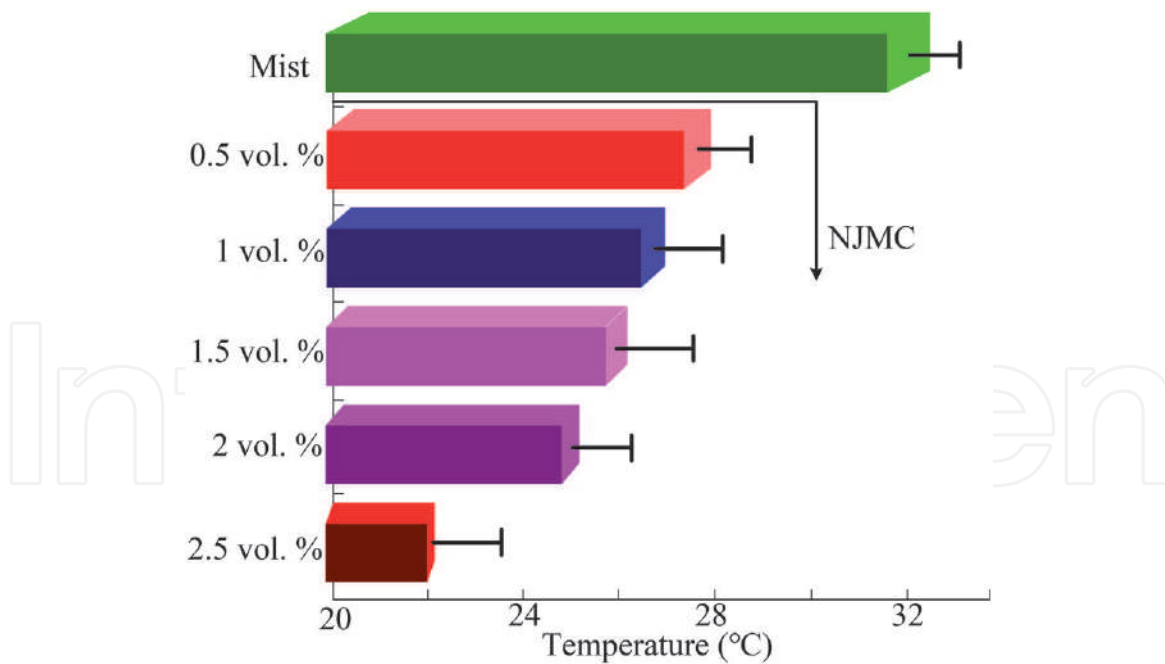


Figure 12.
Temperature values measured with different concentration of nanoparticles.

3.4 Effect of nanoparticle concentration on bone micro grinding temperature

SiO₂ nanofluid with volume fraction of 0.5, 1, 1.5, 2, and 2.5 vol.% was prepared in the experiment to investigate the influence laws of nanoparticle concentration on bone micro grinding temperature. Mist cooling was taken for comparative experiment and to measure grinding force and temperature at measuring point T2.

As shown in **Figure 12**, the temperature measured under mist cooling is 32.7°C. Mist cooling is taken for control, and the surface temperature obtained using nanofluid with volume fraction of 0.5, 1, 1.5, 2, and 2.5 vol.% declines by 14.1%, 17.1%, 19.6%, 22.9%, and 33.3%, respectively, namely the surface temperature in micro grinding decreases as the nanoparticle volume fraction increases.

4. Conclusions

As irreversible thermal injury and poor visibility of operative region exist in the current clinical bone micro grinding operation, a NJMC bio-bone micro grinding process has been proposed to investigate the convective heat transfer mechanism of nanofluid in the grinding zone and reveal the heat distribution mechanism. On this basis, a dynamic temperature field model in NJMC bio-bone micro grinding process has been established. An experimental platform of NJMC bio-bone micro grinding process has been set up to realize an experimental verification of dynamic temperature fields in this grinding process, followed by an experimental study of influence of laws of nanoparticle size and concentration on bone grinding temperature. The following conclusions are drawn:

1. Heat distribution coefficient of specimen material, that of abrasive particle, that of grinding chips, and that of cooling medium, characterizes the abilities of heat transfer media to contend for heat quantity in the unit area of the grinding zone within unit time, so the heat distribution coefficient of the

specimen material can be expressed as the function of heat transfer coefficient of each heat transfer medium in the micro grinding zone.

2. Compared with average temperature (36.8°C) on bone surface under dry grinding condition, bone surface temperatures under mist cooling and NJMC conditions decrease by 13.6% and 33.9%, respectively, thus verifying the superior cooling effect of NJMC. The temperature error is 6.7%, theoretical analysis basically accords with experimental result, and thus the correctness of temperature field in NJMC bio-bone micro grinding is proved.
3. Al₂O₃ nanoparticles with different particle sizes and NS were employed to prepare nanofluids for bone grinding experiment. According to the experimental results, the grinding temperature rose abruptly at entry end of the contact zone, the peak temperature value deviated from the central position of heat source on the curve and deflected toward the exit end of the contact zone, the temperature at the exit end of the contact zone declined slowly, and the grinding temperature increased with the nanoparticle size.
4. The bone grinding experiment has been carried out with nanofluids prepared using SiO₂ nanoparticles with different volume fractions and NS. In comparison with mist cooling, the surface temperatures obtained through nanofluids with nanoparticle volume fraction of 0.5, 1, 1.5, 2, and 2.5 vol.% declined by 14.1%, 17.1%, 19.6%, 22.9%, and 33.3%, respectively, namely the surface temperature declined as the nanoparticle volume fraction increased in grinding.

Acknowledgements

This research was financially supported by the following organizations: the National Natural Science Foundation of China (51975305 and 51905289), the Major Research Project of Shandong Province (2019GSF108236, 2019GGX104040, and 2018GGX103044), the Shandong Provincial Natural Science Foundation of China (ZR2019PEE008), Major Science and Technology Innovation Engineering Projects of Shandong Province (2019JZZY020111), and Applied Basic Research Youth Project of Qingdao Science and Technology Plan (19-6-2-63-cg).

Conflict of interests

The authors confirm that no conflict of interest exists in this chapter.

Appendices and nomenclature

NJMC	nanoparticle jet mist cooling
T_w	set temperature at boundary surface
NS	normal saline
Q_w	heat quantity passing through boundary surface
3D	three-dimensional
q_w	convective heat flux at the boundary surface
T	grinding temperature
h	convective heat transfer coefficient at the boundary between cooling heat transfer medium and specimen

x, y, z	spatial coordinates
b_g	width of grinding tool
t	time
q_w	heat quantity staying on the specimen surface
l_c	contact arc length
q_g	heat quantity transferred into abrasive particle of grinding tool
Q	the heat quantity passing through infinitesimal isothermal surface
q_c	heat quantity carried away by grinding chips
q_x	heat flux in direction x
q_f	heat quantity transferred out by cooling medium
ρ	density of point heat source heat conducting medium
T_{\max}	maximum contact temperature
c	specific heat of point heat source heat conducting medium
T_b	boiling point of grinding fluid
α_t	thermal diffusion coefficient of point heat source heat conducting medium
T_m	melting point of specimen
l	isometric spatial step length
h_w	heat transfer coefficients of specimen material
l_w	specimen length
h_g	heat transfer coefficients of grinding tool
b_w	specimen height
h_f	heat transfer coefficients of grinding fluid
M, N	natural numbers
h_d	heat transfer coefficients of grinding chips
s_f	convection heat transfer boundary surface
R_w	the proportion of heat quantity flowing into the specimen

IntechOpen

IntechOpen

Author details

Min Yang¹, Changhe Li^{1*}, Liang Luo², Lan Dong³, Dongzhou Jia⁴, Runze Li⁵, Mingzheng Liu¹, Xin Cui¹, Yali Hou¹, Yanbin Zhang¹, Teng Gao¹, Xiaoming Wang¹ and Yunze Long^{6*}

1 School of Mechanical and Automotive Engineering, Qingdao University of Technology, Qingdao, China

2 Ningbo Sanhan Alloy Material Co., Ltd, Ningbo, China

3 School of Mechanical and Electrical Engineering, Qingdao Binhai University, Qingdao, China

4 School of Mechanical Engineering, Inner Mongolia University for Nationalities, Tongliao, China

5 Department of Biomedical Engineering, University of Southern California, Los Angeles, United States

6 School of Physical Sciences, Qingdao University, Qingdao, China

*Address all correspondence to: sy_lichanghe@163.com and yunze.long@163.com

IntechOpen

© 2020 The Author(s). Licensee IntechOpen. Distributed under the terms of the Creative Commons Attribution - NonCommercial 4.0 License (<https://creativecommons.org/licenses/by-nc/4.0/>), which permits use, distribution and reproduction for non-commercial purposes, provided the original is properly cited. 

References

- [1] Lee PH, Lee SW, Lim SH, et al. A study on thermal characteristics of micro-scale grinding process using nanofluid minimum quantity lubrication (MQL). *International Journal of Precision Engineering and Manufacturing*. 2015;**16**(9):1899-1909. DOI: 10.1007/s12541-015-0247-2
- [2] Feldmann A, Ganser P, Nolte L, et al. Orthogonal cutting of cortical bone: Temperature elevation and fracture toughness. *International Journal of Machine Tools and Manufacture*. 2017; **118-119**:1-11. DOI: 10.1016/j.ijmachtools.2017.03.009
- [3] Zhang L, Tai BL, Wang AC, et al. Mist cooling in neurosurgical bone grinding. *CIRP Annals - Manufacturing Technology*. 2013;**62**(1):367-370. DOI: 10.1016/j.cirp.2013.03.125
- [4] Jia DZ, Li CH, Zhang YB, et al. Experimental evaluation of surface topographies of NMQL grinding ZrO₂ ceramics combining multiangle ultrasonic vibration. *The International Journal of Advanced Manufacturing Technology*. 2019;**100**(1-4):457-473. DOI: 10.1007/s00170-018-2718-y
- [5] Yang M, Li CH, Zhang YB, et al. Effect of friction coefficient on chip thickness models in ductile-regime grinding of zirconia ceramics. *The International Journal of Advanced Manufacturing Technology*. 2019; **102**(5):2617-2632. DOI: 10.1007/s00170-019-03367-0
- [6] Yang M, Li CH, Zhang YB, et al. Predictive model for minimum chip thickness and size effect in single diamond grain grinding of zirconia ceramics under different lubricating conditions. *Ceramics International*. 2019;**45**(12):14908-14920. DOI: 10.1016/j.ceramint.2019.04.226
- [7] Yang M, Li CH, Zhang YB, et al. Maximum undeformed equivalent chip thickness for ductile-brittle transition of zirconia ceramics under different lubrication conditions. *International Journal of Machine Tools and Manufacture*. 2017;**122**:55-65. DOI: 10.1016/j.ijmachtools.2017.06.003
- [8] Zhang YB, Li CH, Yang M, et al. Experimental evaluation of cooling performance by friction coefficient and specific friction energy in nanofluid minimum quantity lubrication grinding with different types of vegetable oil. *Journal of Cleaner Production*. 2016;**139**: 685-705. DOI: 10.1016/j.jclepro.2016.08.073
- [9] Wu WT, Li CH, Yang M, et al. Specific energy and g ratio of grinding cemented carbide under different cooling and lubrication conditions. *The International Journal of Advanced Manufacturing Technology*. 2019;**105** (1-4):67-82. DOI: 10.1007/s00170-019-04156-5
- [10] Jia DZ, Li CH, Zhang YB, et al. Experimental research on the influence of the jet parameters of minimum quantity lubrication on the lubricating property of Ni-based alloy grinding. *International Journal of Advanced Manufacturing Technology*. 2016;**82**: 617-630. DOI: 10.1007/s00170-015-7381-y
- [11] Zhang YB, Li CH, Ji HJ, et al. Analysis of grinding mechanics and improved predictive force model based on material-removal and plastic-stacking mechanisms. *International Journal of Machine Tools and Manufacture*. 2017;**122**: 81-97. DOI: 10.1016/j.ijmachtools.2017.06.002
- [12] Cui X, Li CH, Zhang YB, et al. Tribological properties under the grinding wheel and workpiece interface by using graphene nanofluid lubricant. *The International Journal of Advanced*

Manufacturing Technology. 2019;**104**
(9–12):3943-3958

[13] Zhang LH, Tai BL, Wang GJ, et al. Thermal model to investigate the temperature in bone grinding for skull base neurosurgery. *Medical Engineering & Physics*. 2013;**35**(10):1391-1398. DOI: 10.1016/j.medengphy.2013.03.023

[14] Zhu Z, Hu ZW, Zhang ZB, et al. Study on grinding force of bovine cortical bone by different grinding wheels. *Diamond & Abrasives Engineering*. 2014;**34**(5):13-16

[15] Sasaki M, Morris S, Goto T, et al. Spray-irrigation system attached to high-speed drills for simultaneous prevention of local heating and preservation of a clear operative field in spinal surgery. *Neurologia Medico-Chirurgica*. 2010;**50**(10):900-904. DOI: 10.2176/nmc.50.900

[16] Enomoto T, Shigeta H, Sugihara T, et al. A new surgical grinding wheel for suppressing grinding heat generation in bone resection. *CIRP Annals - Manufacturing Technology*. 2014;**63**(1): 305-308. DOI: 10.1016/j.cirp.2014.03.026

[17] Zhang XM, Ren ZP, Mei FM. *Heat Transfer*. Beijing: China Construction Industry Press; 1995. pp. 75-96

[18] Jaeger JC. Moving sources of heat and the temperature of sliding contacts. *Proceedings of the Royal Society of New South Wales*. 1942;**76**:203-224

[19] Li HN, Xie KG, Wu B, et al. Generation of textured diamond abrasive tools by continuous-wave CO₂ laser: Laser parameter effects and optimisation. *Journal of Materials Processing Technology*. 2020;**275**: 116279. DOI: 10.1016/j.jmatprotec.2019.116279

[20] Li HN, Yang Y, Zhao YJ, et al. On the periodicity of fixed-abrasive planetary lapping based on a generic

model. *Journal of Manufacturing Processes*. 2019;**44**:271-287. DOI: 10.1016/j.jmapro.2019.05.036

[21] Yang M, Li CH, Zhang YB, et al. Experimental research on microscale grinding temperature under different nanoparticle jet minimum quantity cooling. *Materials and Manufacturing Processes*. 2016;**32**:589-597. DOI: 10.1080/10426914.2016.1176198

[22] Gao T, Zhang XP, Li CH, et al. Surface morphology evaluation of multi-angle 2D ultrasonic vibration integrated with nanofluid minimum quantity lubrication grinding. *Journal of Manufacturing Processes*. 2020;**51**:44-61. DOI: 10.1016/j.jmapro.2020.01.024

[23] Zhang DK, Li CH, Zhang YB, et al. Experimental research on the energy ratio coefficient and specific grinding energy in nanoparticle jet MQL grinding. *International Journal of Advanced Manufacturing Technology*. 2015;**78**:1275-1288. DOI: 10.1007/s00170-014-6722-6

[24] Shen B. *Minimum Quantity Lubrication Grinding Using Nanofluids*. Michigan: The University of Michigan; 2008

[25] Malkin S, Guo C. Thermal analysis of grinding. *CIRP Annals - Manufacturing Technology*. 2007;**56**(2):760-782

[26] Kuwahara F, Shirota M, Nakayama A. A numerical study of interfacial convective heat transfer coefficient in two-energy equation model for convection in porous media. *International Journal of Heat and Mass Transfer*. 2001;**44**(6):1153-1159. DOI: 10.1016/s0017-9310(00)00166-6

[27] Duursma G, Sefiane K, Kennedy A. Experimental studies of nanofluid droplets in spray cooling. *Heat Transfer Engineering*. 2009;**30**(13):1108-1120. DOI: 10.1080/01457630902922467

- [28] Zhang DK, Li CH, Jia DZ, et al. Specific grinding energy and surface roughness of nanoparticle jet minimum quantity lubrication in grinding. *Chinese Journal of Aeronautics*. 2015;**28**(2): 570-581. DOI: 10.1016/j.cja.2014.12.035
- [29] Li HN, Axinte D. On a stochastically grain-discretised model for 2D/3D temperature mapping prediction in grinding. *International Journal of Machine Tools and Manufacture*. 2017; **116**:60-76. DOI: 10.1016/j.ijmachtools.2017.01.004
- [30] Yang SM, Tao WS. *Heat Transfer*. Higher Education Press: Beijing; 1998. pp. 33-296p
- [31] Outwater JQ, Shaw MC. Surface temperature in grinding. *ASME*. 1952; **12**(1):73-78
- [32] Rowe WB, Black SCE, Mills B, et al. Analysis of grinding temperatures by energy partitioning. *Proceedings of the Institution of Mechanical Engineers, Part B: Journal of Engineering Manufacture*. 1996;**210**(6):579-588
- [33] Yang YH, Liu CH, Liang YH, et al. Hollow mesoporous hydroxyapatite nanoparticles (hmHANPs) with enhanced drug loading and pH-responsive release properties for intracellular drug delivery. *Journal of Materials Chemistry B*. 2013;**1**(19): 2447-2450. DOI: 10.1039/c3tb20365d
- [34] Deng H, Lei Z. Preparation and characterization of hollow $\text{Fe}_3\text{O}_4/\text{SiO}_2@$ PEG-PLA nanoparticles for drug delivery. *Composites Part B: Engineering*. 2013;**54**:194-199. DOI: 10.1016/j.compositesb.2013.05.010
- [35] Yang M, Li CH, Zhang YB, et al. Theoretical analysis and experimental research on temperature field of microscale bone grinding under nanoparticle jet mist cooling. *Journal of Mechanical Engineering*. 2018;**54**(18): 194-203. DOI: 10.3901/JME.2018.18.194
- [36] Yang M, Li CH, Zhang YB, et al. Thermodynamic mechanism of Nanofluid minimum quantity lubrication cooling grinding and temperature field models. In: Mohsen Sheikholeslami Kandelousi, *Microfluidics and Nanofluidics*. London: IntechOpen; 2018. pp. 61-81
- [37] Zhang YB, Li CH, Jia DZ, et al. Experimental evaluation of the lubrication performance of MoS_2/CNT nanofluid for minimal quantity lubrication in Ni-based alloy grinding. *International Journal of Machine Tools and Manufacture*. 2015;**99**:19-33. DOI: 10.1016/j.ijmachtools.2015.09.003
- [38] Gao T, Li CH, Zhang YB, et al. Dispersing mechanism and tribological performance of vegetable oil-based CNT nanofluids with different surfactants. *Tribology International*. 2019;**131**:51-63. DOI: 10.1016/j.triboint.2018.10.025
- [39] Zhang YB, Li CH, Jia DZ, et al. Experimental evaluation of MoS_2 nanoparticles in jet MQL grinding with different types of vegetable oil as base oil. *Journal of Cleaner Production*. 2015; **87**:930-940. DOI: 10.1016/j.jclepro.2014.10.027
- [40] Lee PH, Nam JS, Li C, et al. An experimental study on micro-grinding process with nanofluid minimum quantity lubrication (MQL). *International Journal of Precision Engineering and Manufacturing*. 2012; **13**:331-338. DOI: 10.1007/s12541-012-0042-2
- [41] Yang M, Li CH, Zhang YB, et al. Research on microscale skull grinding temperature field under different cooling conditions. *Applied Thermal Engineering*. 2017;**126**:525-537. DOI: 10.1016/j.applthermaleng.2017.07.183

Material Removal Mechanism and Force Model of Nanofluid Minimum Quantity Lubrication Grinding

Yanbin Zhang, Changhe Li, Yongjun Zhao, Xin Cui, Xiufang Bai, Mingzheng Liu, Yali Hou, Min Yang, Naiqing Zhang, Heju Ji, Xiaoming Wang and Teng Gao

Abstract

Numerous researchers have developed theoretical and experimental approaches to force prediction in surface grinding under dry conditions. Nevertheless, the combined effect of material removal and plastic stacking on grinding force model has not been investigated. In addition, predominant lubricating conditions, such as flood, minimum quantity lubrication (MQL), and nanofluid minimum quantity lubrication (NMQL), have not been considered in existing force models. In this study, material removal mechanism under different lubricating conditions was researched. An improved theoretical force model that considers material removal and plastic stacking mechanisms was presented. Grain states, including cutting and ploughing, are determined by cutting efficiency (β). The influence of lubricating conditions was also considered in the proposed force model. Simulation was performed to obtain the cutting depth (a_g) of each “dynamic active grain.” Parameter β was introduced to represent the plastic stacking rate and determine the force algorithms of each grain. The aggregate force was derived through the synthesis of each single-grain force. Finally, pilot experiments were conducted to test the theoretical model. Findings show that the model’s predictions were consistent with the experimental results, with average errors of 4.19% and 4.31% for the normal and tangential force components, respectively.

Keywords: grinding, minimum quantity lubrication, nanofluid, material removal mechanism, force model

1. Introduction

With need of green manufacturing, nanofluid minimum quantity lubrication (NMQL) was introduced to grinding [1, 2], which could effectively improve cooling and lubricating performance compared to conventional dry or flood conditions [3, 4]. Furthermore, with the deeper understanding of grinding mechanism and the development of process technology for difficult-to-grinding material, advancement in the experiment has been rapidly made [5–7]. Of course, with such a demand from

designing of grinding technological parameter, material removal mechanism and force model under NMQL condition are of key importance.

Material removal mechanism, here, mostly refers to deformation, fracture process, and strain rate of material in grinding zone, as well as mechanical behavior of chips and furrow formation [8, 9], which relates to grinding parameters and cooling/lubricating conditions [10, 11]. For dry grinding, the experimental studies have been carried out, and force, temperature, shape of chips, and surface quality were observed, which showed special phenomenon when higher speed (i.e., speed effect) and lower cutting depth (i.e., size effect) were used. Nevertheless, material removal mechanism under NMQL condition is vacant and important, which should be researched deeply.

Force model of grinding, in general, was vector sum of sliding force, cutting force, and ploughing force of all dynamic active grains in grinding zone. Many researches were carried out to establish grinding force model under dry condition. Werner [12] derived a grinding force equation with two parts (cutting force and sliding force), which was adopted by Malkin and Hwang [13], Li et al. [14], Younis et al. [15], and Tang et al. [16]. To obtain grain stages and numbers, Rayleigh's probability density distribution [17, 18] and normal distribution [19] were used to describe cutting depth of grain [20]. Except for steel material, the grinding force model was also researched for single crystal sapphire [21], SiCp/Al composites [22], complex optical mirrors [23], etc. However, previous models were limited at three aspects:

- i. The average cutting depths were used for each grain states (i.e., cutting, ploughing, sliding), which cannot represent the actual situation in the grinding zone [24].
- ii. The critical depth of cutting and ploughing was determined by an experience-based evaluation method: "when the grain-cutting depth reached 0.05 times of the radius of cutting grains, cutting action occurred" [25–27]. It's imprecise for different material.
- iii. The number of "static active grains" was presented to develop force models, which are not considered interference effect of grains on each other [28–32].
- iv. The lubricating condition was not considered.

This chapter proposes an improved theoretical force model that takes the material removal and plastic stacking mechanism into consideration. The scratch tests reveal the relationship between cutting depth (a_g) and cutting efficiency (β) to distinguish the cutting and ploughing grains and determine the force algorithms of each grain. The tribological tests reveal the friction coefficients under different grinding lubricating conditions to calculate the frictional force of each grain. In addition, the a_g of each "dynamic active grain" in the grinding zone is obtained by simulation, to assist the development of the grinding force model. To verify the proposed model, grinding experiments were performed, and force values were obtained and compared with predictive values.

2. Material removal mechanism of NMQL grinding

2.1 Deformation and strain rate

The material deformation mechanism in the grinding zone with single abrasive particle is shown in **Figure 1**. The material deformation mechanism in the chip

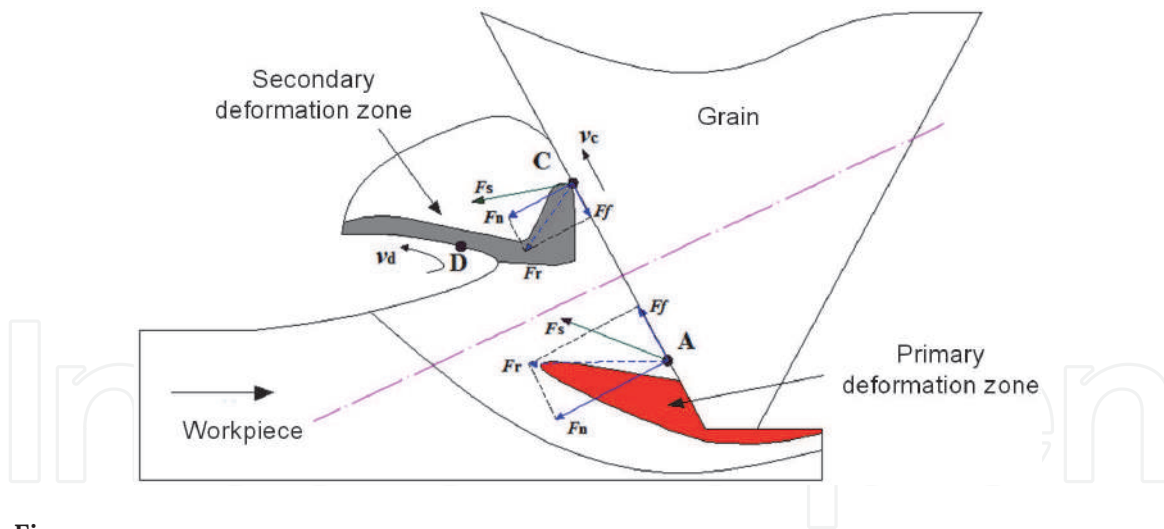


Figure 1.
 Deformation mechanism of material in the cutting zone.

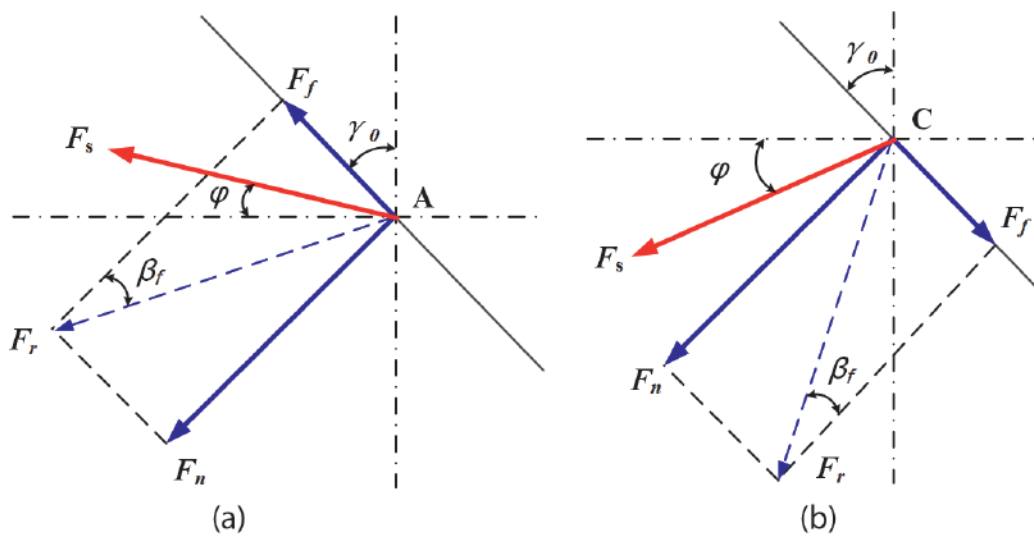


Figure 2.
 Stress analysis of the workpiece material in the cutting zone. (a) Primary deformation zone and (b) secondary deformation zone.

formation zone during the grinding machining is identical with that during cutting machining, and primary deformation zone and secondary deformation zone simultaneously exist.

Ding et al. [33] conducted an analog simulation of high-temperature cutting of nickel-based alloy workpiece material with single abrasive particle and also observed the abovementioned phenomenon. Different from cutting machining, the negative rake cutting form of abrasive particle leads to a different mechanical action mechanism between abrasive particle/grinding chips; the calculation formulas of shear angle φ , frictional angle β_f , and strain rate are also changed, but the impact trends of grinding process parameters and lubricating conditions on material removal mechanism are totally the same. The force analysis of the grinding zone of single abrasive particle is shown in **Figure 2**, and material force bearing and deformation mechanism can be described as follows:

- i. In the primary deformation zone, **Figure 2(a)** is force analysis graph of point A, and the resultant force of frictional force F_f and extrusion force F_n is F_r . According to the mechanical theory of material, the included angle between rupture chip formation direction (direction F_s of shear zone) and resultant force F_r is $\pi/4$, and shear angle φ is on horizontal line; at the time, frictional force F_f

exerts a promoting effect on rupture chip formation of the material upward along the abrasive particle/cutting chip interface. Hence, the expression of shear angle φ is solved according to geometrical relations of several angles as below:

$$\varphi_1 = \frac{\pi}{4} + \beta_f - \gamma_0 \quad (1)$$

The ratio of thickness to length of grinding chips formed through cutting machining of abrasive particle is about 1/100, so negative rake is $\gamma_0 \approx \theta/2$ and frictional angle is $\beta_f = \arctan(\mu)$ under abrasive particle cutting, where μ is frictional coefficient between rake face of abrasive particle/cutting chips. The relational expression between γ_0 and β is substituted into Eq. (1) to obtain:

$$\varphi_1 = \frac{\pi}{4} + \arctan \mu - \frac{\theta}{2} \quad (2)$$

- ii. In the secondary deformation zone, **Figure 2(b)** is force analysis chart, where the resultant force of frictional force F_f and extrusion force F_n is F_r . According to the mechanical theory of material, the included angle between rupture chip formation direction (direction F_s of shear zone) and resultant force F_r is $\pi/4$, and shear angle φ is below the horizontal line; at the time, frictional force F_f exerts an inhibitory effect on flow of grinding chips downward along the abrasive particle/cutting chip interface. After kinetic analysis, speed of movement on abrasive particle/grinding chip interface is low due to frictional force, but the speed on free face of grinding chips is high; under high-speed cutting condition, transient speed difference is generated between abrasive particle/grinding chip interface and free face of grinding chips due to high strain rate of grinding chips, thus generating a shear zone and forming the secondary deformation zone. Hence, the expression of shear angle φ can be solved according to geometrical relations of several angles as:

$$\phi_2 = \beta_f + \gamma_0 - \frac{\pi}{4} = \arctan \mu + \frac{\theta}{2} - \frac{\pi}{4} \quad (3)$$

For high-speed grinding machining, the change of strain rate is the primary factor influencing the material removal mechanism. The strain rate reaches as high as 10^4 – 10^5 s^{-1} in the cutting machining process, but for low-speed grinding machining ($V_s \leq 30 \text{ m/s}$), the strain rate of material removal reaches up to 10^7 – 10^8 s^{-1} because of negative rake characteristic of abrasive particle. Therefore, it's speculated that the strain rate under high-speed grinding machining condition is higher than that under low-speed grinding machining condition of grinding wheel by 1 or 2 orders of magnitudes. Under high-speed grinding machining condition, the strain hardening effect and strain strengthening effect caused by strain rate of material deformation generate a remarkable effect on the material removal mechanism. Jin and Stephenson [34] established the equation of shear strain in the shear zone of abrasive particle and strain rate. Taking maximum undeformed cutting thickness and shear angle in the primary deformation zone and secondary deformation zone into account, strain rate of grinding chips in the two deformation zones could be calculated by the following equations:

$$\dot{\gamma}_1 = \frac{\lambda v_s^2 \cos\left(\frac{\theta}{2}\right) \sin\left(\frac{\pi}{4} + \arctan \mu - \frac{\theta}{2}\right)}{\pi v_w \sqrt{a_p D} \cos\left(\frac{\pi}{4} + \arctan \mu\right)} \quad (4)$$

$$\gamma_2 = - \frac{\lambda v_s^2 \cos\left(\frac{\theta}{2}\right) \sin\left(\arctan \mu + \frac{\theta}{2} - \frac{\pi}{4}\right)}{\pi v_w \sqrt{a_p D} \cos\left(\arctan \mu + \theta - \frac{\pi}{4}\right)} \quad (5)$$

where φ is shear angle, θ is vertex angle of abrasive particle, λ_1 is average length-width ratio in the shear zone ($\lambda_1 = 6-12$), v is cutting speed of abrasive particle, and $v \approx V_s$ is for single abrasive particle grinding.

It can be known from Eq. (4) that factors influencing deformational strain rate of workpiece material during the cutting process with single abrasive particle include grinding parameters, abrasive particle shape, and lubrication characteristics of abrasive particle/grinding chip interface. In this study, as $V_s/V_w = 1 \times 10^4$ and abrasive particle shape are unchanged, the influence trends of grinding speed V_s , grinding depth V_w , and grinding coefficient μ on shear rate will be hereby discussed.

As shown in **Figure 3(a)**, when other parameters remain unchanged, the strain rates in both primary shear zone and secondary shear zone present a linear growth trend when V_s increases from 30 to 120. In comparison with the primary deformation zone, the strain rate in the secondary deformation zone has a higher growth rate.

According to **Figure 3(b)**, when the frictional coefficient μ gradually increases, the strain rate in the primary deformation zone presents an increasing trend of quadratic function, because the frictional force in the primary deformation zone exerts a gaining effect on material removal and the strain rate increases with frictional force, which is better for chip formation. In the secondary deformation zone, as the frictional coefficient μ increases from small to great (characterizing lubricating condition), the strain

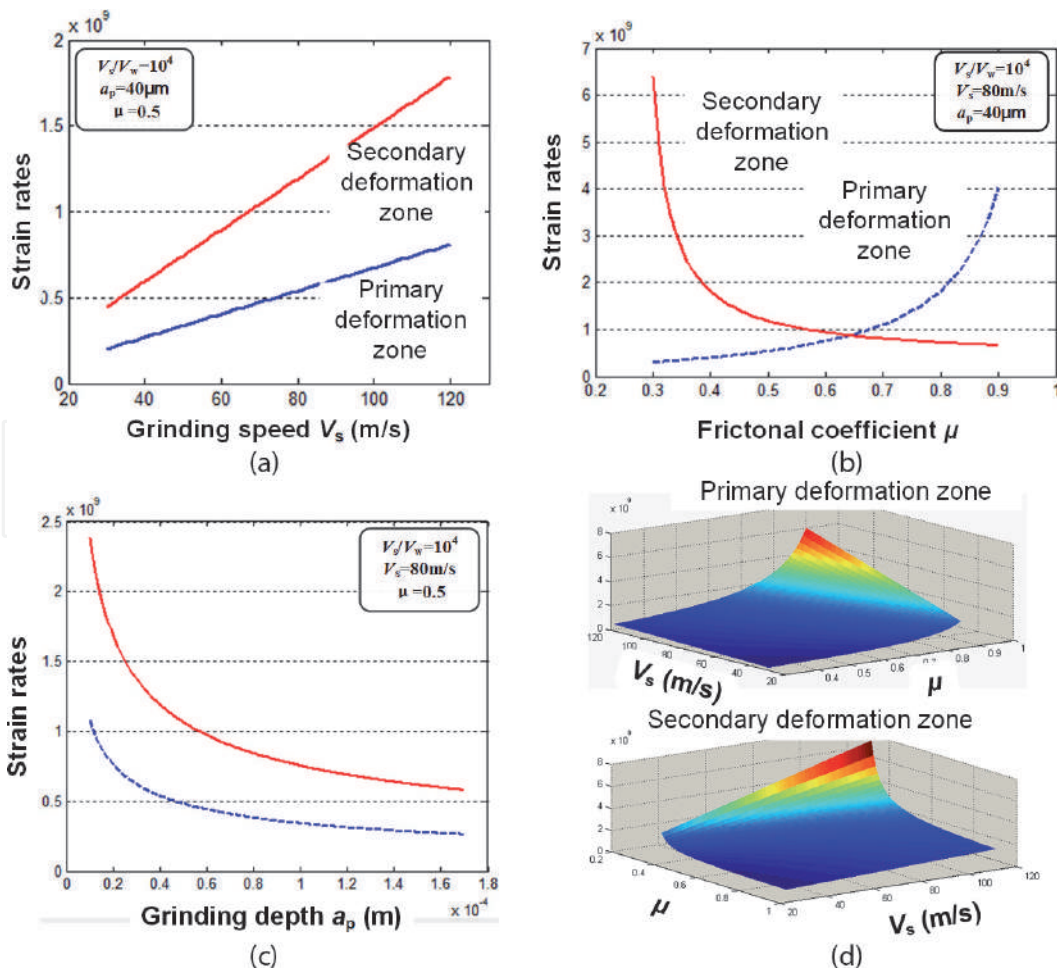


Figure 3. Strain rate under different grinding parameters and frictional coefficient. (a) Influence of grinding speed, (b) influence of frictional coefficient, (c) influence of grinding depth and (d) two-factor analysis.

rate in the secondary deformation zone presents a declining trend of quadratic function, the frictional force in the primary deformation zone prevents grinding chips from flowing out, and flow direction of grinding chips is gradually turned from towards abrasive particle into along the surface of abrasive particle, so the strain rate gradually declines. As shown in **Figure 3(c)**, the strain rate presents a linear declining trend due to increase of grinding depth. As this study focuses on speed effect and lubricating effect in the high-speed grinding machining, in consideration of impact trends of grinding speed and frictional coefficient on strain rate, **Figure 3(d)** shows the variation trend graphs of the primary deformation zone and secondary deformation zone under the influence of grinding speed and frictional coefficient.

2.2 Mechanism of chip formation

2.2.1 Theoretical research

Impact dynamics describes material deformation behaviors under high speed as an adiabatic shear process. Adiabatic shear effect refers to constitutive instability (thermal viscoplastic instability) of the material under impact load. Extremely strain rate exists in the material removal shear zone under the action of impact load, and the shear zone is a thermal insulating environment within a very short time. At the time, nonelastic energy in the material deformation process is converted into a large quantity of grinding heat, which leads to abrupt temperature rise of the material in the shear zone and declination of material hardness (softening) under temperature rise. The softening effect exceeds strain hardening effect and strain strengthening effect, and thus shear zone is formed and material instability is caused. Hence, the chip formation process under the effect of abrasive particle is dynamic stress and thermal force coupling action process under a high strain rate.

The removal process of metal material derives from plastic deformation after the material strain increases. In the previous studies, scholars have conducted a large quantity of dynamic material tensile tests [35], proving strain hardening and strain strengthening phenomena. As shown in **Figure 4**, the material removal process with the change of strain rate can be divided into the three following types according to the stress-strain curve:

As shown in **Figure 5(a)**, under quasi-static conditions, the material deformation stress will increase obviously with the strain, indicating that notable strain hardening effect happens to the workpiece material. Grinding chips will be formed after the stress increases to material breaking limit σ_{b1} , and free face of cutting chips presents periodic upheaval (bamboo shape), which is caused by extruding deformation in the grinding chip formation process; however, the strain rate of material deformation is low because of low speed, and no obvious shear zone is formed.

As shown in **Figure 5(b)**, under high strain rate, assume that the shear zone of grinding chips is in an isothermal environment: the material deformation stress in the strain hardening phase is far higher than that under quasi-static conditions, and this phenomenon is called “strain strengthening effect” of plastic deformation of material, and its deformational resistance is enhanced under strain strengthening effect. At the time, as abrasive particle has a strong impact effect on the material, workpiece material forms shear layers under high strain rate so as to form grinding chips, and rupture stress limit between shear layers is breaking limit σ_{b2} of the material under high strain rate. Free face of grinding chips presents notable periodic shear slippage layer, and the slippage distance of shear layer under high strain condition is obviously higher than that under quasi-static state; and the higher the speed, the higher the strain rate, and the greater the slippage distance of shear layer; and even radical rupture and separation between shear layers is caused by bluff-type rupture process.

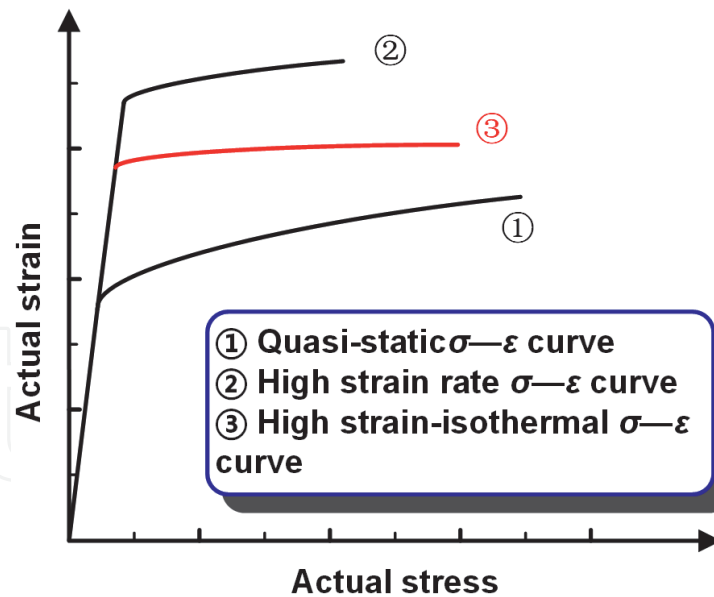


Figure 4.
 Stress-strain curve under “velocity effect.”

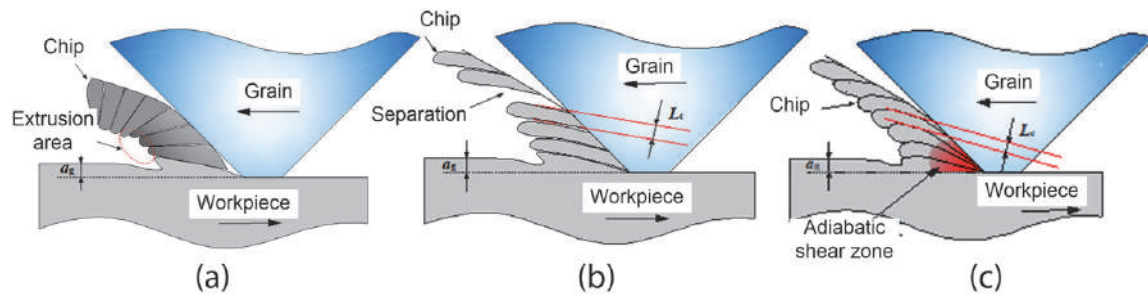


Figure 5.
 Chip-forming mechanism under (a) quasi-static, (b) high strain isothermal, and (c) high strain condition.

As shown in **Figure 5(c)**, in consideration of temperature rise at abrasive particle/grinding chip interface under high strain rate, the plastic deformation process of the material at the time is a comprehensive result of strain hardening effect and thermal softening effect, namely, adiabatic shear process. In **Figure 4**, the stress-strain curve is between quasi-static curve (curve 1) and high strain isothermal condition (curve 2) under the action of adiabatic shear, because a large quantity of grinding heat softens the material so as to reduce deformational resistance under the action of strengthening strain rate. As the strain rate increases, the heat transferred to shear zone is also increasing, thermal softening effect becomes more obvious, and the breaking limit relation of the material under three boundary conditions is $\sigma_{b2} > \sigma_{b3} > \sigma_{b1}$. Material rupture and plastic flow after thermal softening simultaneously exist between shear layers of grinding chips.

Hence, the critical research hotspots regarding material removal mechanism under high-speed grinding conditions are to explore into influences of grinding parameters and lubricating conditions on strain strengthening effect and thermal softening effect and build an evaluation model.

2.2.2 Experimental research

SEM of chips were shown in **Figure 6**.

The grinding chip shapes are similar at the grinding speed of 40 m/s under three different working conditions, namely, continuous banding chips, because the material strain rate is low and thermal softening effect in the grinding zone is small under low grinding speed. When the grinding speed is 80 m/s, obvious shear zones

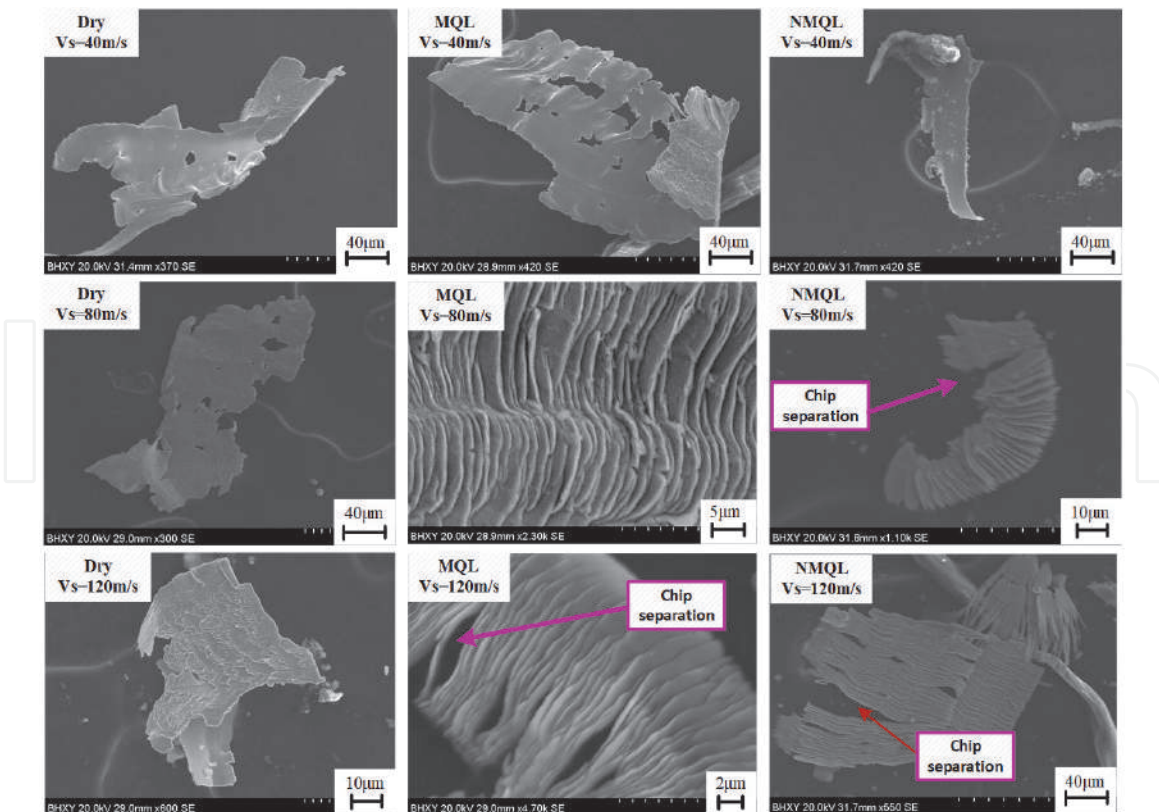


Figure 6.
Chip morphology at different lubricating conditions.

are observed on the free faces of the three types of grinding chips, indicating that under high grinding speed, the material experiences adiabatic shear during the forming process. Differently, the shear slippage layer spacing obtained under dry grinding conditions is small, that under MQL condition is larger, and that under NMQL is the largest, where even rupture takes place.

On the one hand, as the lubricating effect is enhanced and frictional coefficient is reduced in succession under the three lubricating conditions, the strain rate in the primary deformation zone at the same speed increases successively, so does shear slippage distance under the three conditions. On the other hand, the output of frictional heat is reduced as the lubricating effect is enhanced successively under the three conditions, and the heat quantity transferred out of the shear zone is increased as the cooling effect is enhanced successively under the three conditions. Therefore, the thermal softening effect during NMQL cutting chip formation process is lower than that under dry grinding condition. The shear layer slippage of grinding chips is mainly material rupture, followed by plastic flow, so shear layer spacing is larger, and grinding chips even rupture. Under the grinding speed of 120 m/s, the abovementioned rule is magnified again. Banding chips are still formed due to thermal softening effect under dry grinding, rupture of grinding chips induced by excessive shear layer spacing also appears under MQL condition, and the rupture under NMQL condition is further aggravated.

2.3 Mechanism of furrow formation and cutting efficiency

2.3.1 Plastic stacking effect

Cutting depth a_g (varies from 0 to a_{gmax}) and critical value a_{gc} were the key points for distinguishing ploughing and cutting stage. The value a_{gc} could be gotten from cutting experiment of single grain for different materials. The change rule could be concluded from **Figure 7**.

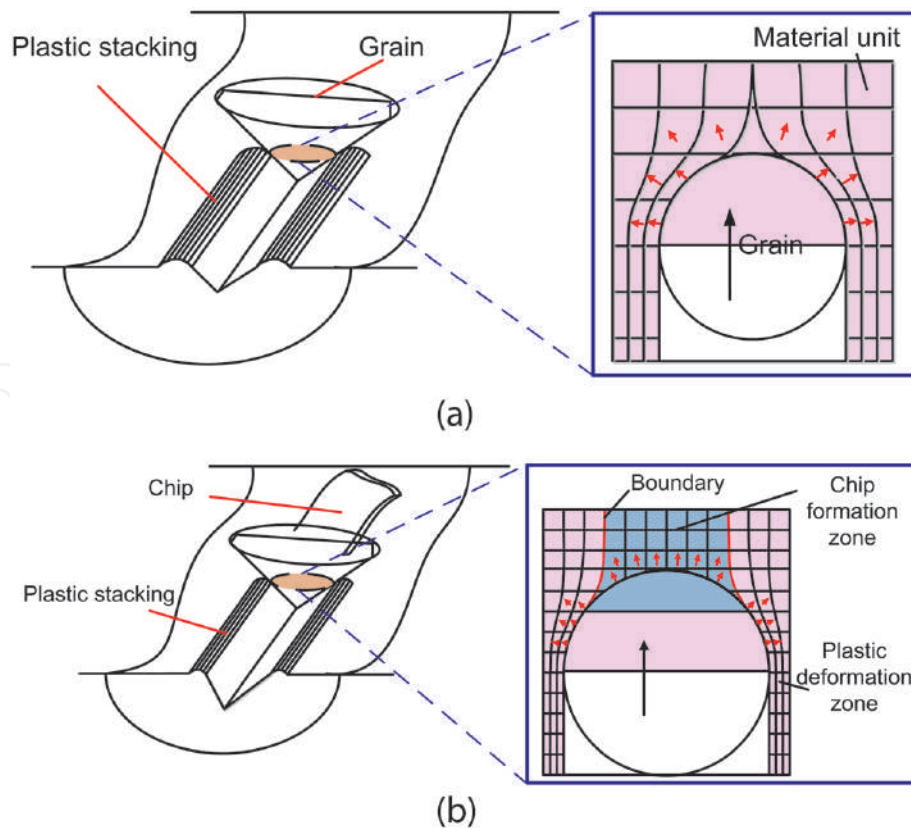


Figure 7. Material deformation behavior in cutting of a single grain. (a) Ploughing grain and (b) cutting grain.

- i. When $a_g \leq a_{gc}$ (ploughing stage). Material of workpiece flows upheaved and stacked at two sides of the furrows because the stress between material units is lower than fracture stress.
- ii. When $a_g > a_{gc}$ (cutting stage). Plastic stacking theory [36], which describes the coexistence phenomenon of material removal and elastic-plastic flow in grinding, is a good method to understand deformation behavior of material. Pink-colored material units in **Figure 7(b)** were the elastic-plastic flow part, and blue-colored units were the material removal part. However, a boundary was born between two regions.

Therefore, chip formation region ($0-\alpha_1$) and elastic-plastic flow region ($\alpha_1-\pi/2$) were defined in this paper, in which two were differentiated by critical value of angle α_1 , as shown in **Figure 8**. α_1 (could be calculated by cutting efficiency β [37]) was different when material changes:

$$\alpha_1 = \arccos(\sqrt{\beta}) \quad (6)$$

2.3.2 Model of $\beta(\alpha_g)$

Parameter β will increase from 0 to almost 1 when a_g increases [38]. Therefore the model of $\beta(\alpha_g)$ is the key point of grinding force prediction. Cutting experiment of single grain was carried out for stainless steel material (440 C, $R_a = 0.04-0.05 \mu\text{m}$). Surface topography of furrow is shown in **Figure 9**, and numerical fitting of $\beta(\alpha_g)$ was shown in **Figure 10**.

The $\beta(\alpha_g)$ curve present S-shaped (when a_g varies from 0 to $4.5 \mu\text{m}$) and further linear trend (when $a_g \geq 4.5 \mu\text{m}$). Therefore, Gompertz growth equation and Gaussian fitting were considered simultaneously, and piecewise function ($R^2 = 0.9945$) is shown as Eq. (7).

$$\beta(a_g) = \begin{cases} a_1 \cdot e^{-\left(\frac{a_g - b_1}{c_1}\right)^2} + a_2 \cdot e^{-\left(\frac{a_g - b_2}{c_2}\right)^2} + \dots + a_6 \cdot e^{-\left(\frac{a_g - b_6}{c_6}\right)^2}, & 0 \leq x \leq 3.8 \mu\text{m} \\ k \cdot e^{-a \cdot e^{-b \cdot a_g}}, & x > 3.8 \mu\text{m} \end{cases} \quad (7)$$

It could be observed from **Figure 10** that (i) three stages could be learned from curve slope of $\beta(\alpha_g)$; (ii) compared to study of Hahn [39], sliding stage (0–0.023 μm) is declined; and (iii) the transition stage exists between ploughing and cutting stage, which is different from traditional theory.

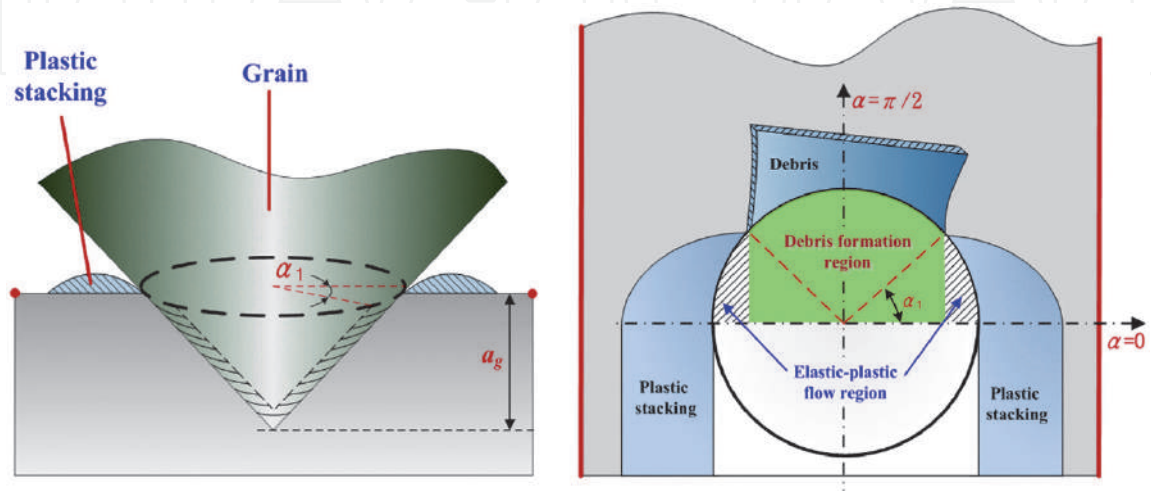


Figure 8.
Plastic stacking mechanism.

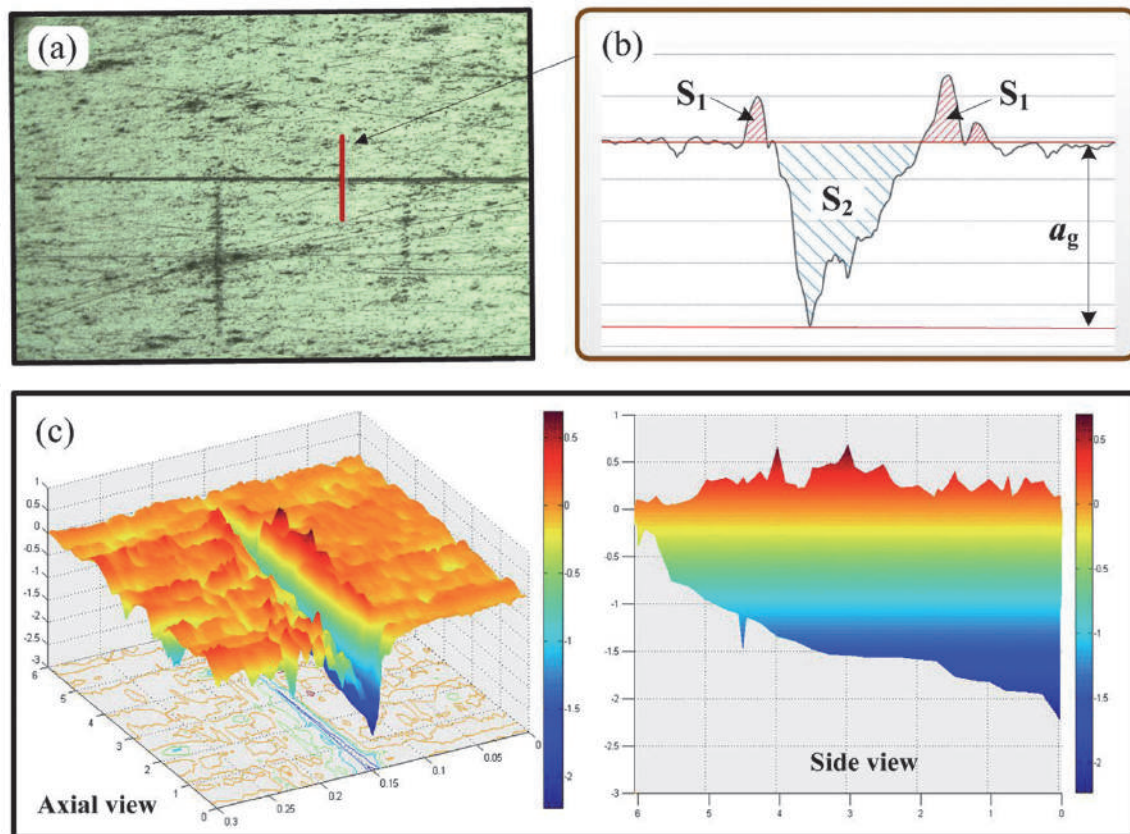


Figure 9.
Result of scratch tests. (a) Surface topography of furrow, (b) 2D profile curve of furrow, (c) 3D graph of furrow.

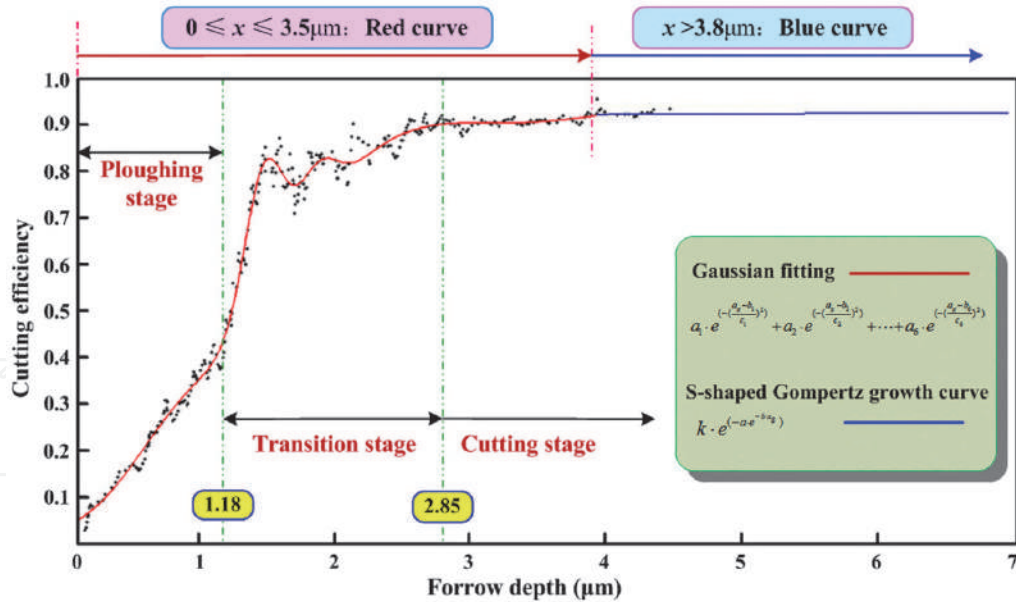


Figure 10.
 Equation of cutting efficiency (β).

3. Force model of single grain

3.1 Stress state of grain

As a premise for force model, analysis of stress state was carried out in this section according to the above results, as shown in **Figure 11**. Plastic flow is the material behavior, and equal stress value (yields stress δ_s) distributes on grain surface. The stresses at chip formation region (δ_0) and elastic-plastic flow region (δ_1) show characteristics as follows: (i) equal stress value (fracture stress δ_b) distributes on chip formation region and (ii) linear formula of stress distributes on elastic-plastic flow region, which varies from 0 to δ_b .

3.2 Force model in chip formation region ($\alpha_1 - \pi/2$)

δ_0 was composed of δ_{01} and δ_{02} in chip formation region. As shown in **Figure 12**, the integral unit (ds) can be expressed as:

$$d_s = \frac{a_g^2 \cdot \tan \theta}{2 \cdot \cos \theta} \cdot d\alpha \quad (8)$$

The plastic flow force equation $F_{tc(01)}(a_g)/F_{nc(01)}(a_g)$ in chip formation region could be calculated as:

$$F_{tc(01)}(a_g) = \int_{\alpha_1}^{\pi} \delta_s \cdot a_g^2 \cdot \tan \theta \cdot \cos \alpha \cdot d\alpha \quad (9)$$

$$F_{nc(01)}(a_g) = \int_{\alpha_1}^{\pi} \delta_s \cdot a_g^2 \cdot \tan^2 \theta \cdot d\alpha = \left(\frac{\pi}{2} - \alpha_1\right) \cdot \delta_s \cdot a_g^2 \cdot \tan^2 \theta \quad (10)$$

where θ is grain vertex angle and α_1 could be obtained by Eqs. (6) and (7), respectively.

The chip formation force equation $F_{tc(02)}(a_g)$ in chip formation region could be calculated as:

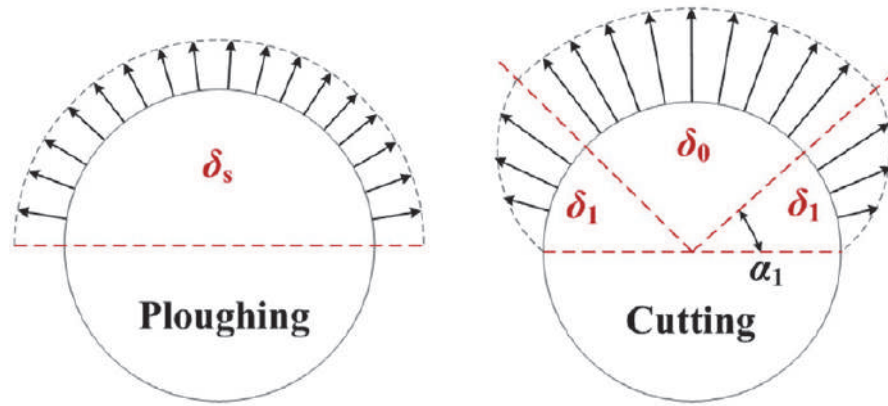


Figure 11. Schematic diagram of the grain stress state.

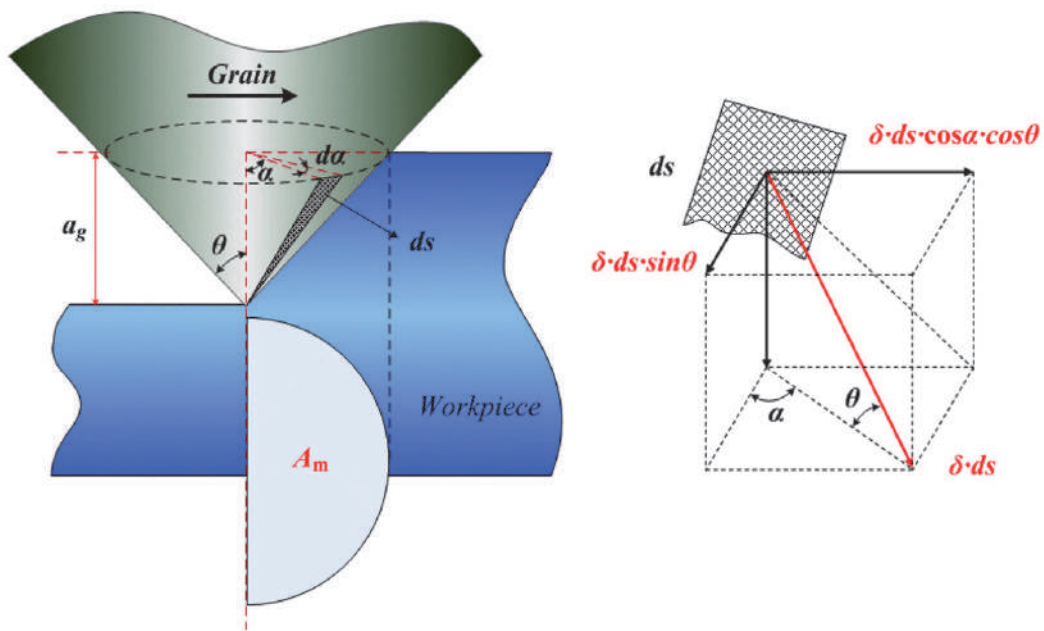


Figure 12. Calculation principle of cutting force.

$$F_{tc(02)}(a_g) = \int_{\alpha_1}^{\frac{\pi}{2}} \delta_{02} \cdot a_g^2 \cdot \tan \theta \cdot \cos \alpha \cdot d\alpha = \delta_b \cdot A_m \quad (11)$$

where A_m is area of the chip formation region and δ_{02} could be obtained by Eq. (11):

$$\delta_{02} = \frac{\pi \cdot \tan \theta}{2 \cdot (1 - \sin \alpha_1)} \cdot \delta_b \quad (12)$$

The normal force could be further calculated by Eqs. (11) and (12):

$$F_{nc(02)}(a_g) = \int_{\alpha_1}^{\frac{\pi}{2}} \delta_{02} \cdot a_g^2 \cdot \tan^2 \theta \cdot d\alpha = \frac{\pi \cdot (\frac{\pi}{2} - \alpha_1)}{2 \cdot (1 - \sin \alpha_1)} \cdot \delta_b \cdot a_g^2 \cdot \tan^3 \theta \quad (13)$$

In summary, δ_0 can be expressed as:

$$\delta_0 = \delta_{01} + \delta_{02} = \delta_s + \frac{\pi \cdot \tan \theta}{2 \cdot (1 - \sin \alpha_1)} \cdot \delta_b \quad (14)$$

3.3 Force model in elastic-plastic flow region (0– α_1)

The equation of δ_1 and force in elastic-plastic flow region show increased trend and could be calculated as:

$$\delta_1(\alpha) = \left[\frac{\delta_s}{\alpha_1} + \frac{\pi \cdot \delta_b \cdot \tan \theta}{\alpha_1 \cdot (1 - \sin \alpha_1)} \right] \cdot \alpha \quad (15)$$

$$F_{ic(1)}(a_g) = \int_0^{\alpha_1} \delta_1(\alpha) \cdot a_g^2 \cdot \tan \theta \cdot \cos \alpha \cdot d\alpha \quad (16)$$

$$F_{nc(1)}(a_g) = \int_0^{\alpha_1} \delta_1(\alpha) \cdot a_g^2 \cdot \tan^2 \theta \cdot d\alpha \quad (17)$$

Force equation of cutting grain could be obtained by the above equation:

$$\begin{aligned} F_{ic}(a_g) &= F_{ic(1)}(a_g) + F_{ic(01)}(a_g) + F_{ic(02)}(a_g) \\ &= \int_0^{\alpha_1} \delta_1(\alpha) \cdot a_g^2 \cdot \tan \theta \cdot \cos \alpha \cdot d\alpha + \int_{\alpha_1}^{\frac{\pi}{2}} \delta_s \cdot a_g^2 \cdot \tan \theta \cdot \cos \alpha \cdot d\alpha + \delta_b \cdot A_m \end{aligned} \quad (18)$$

$$\begin{aligned} F_{nc}(a_g) &= F_{nc(1)}(a_g) + F_{nc(01)}(a_g) + F_{nc(02)}(a_g) \\ &= \left[\int_0^{\alpha_1} \delta_1(\alpha) \cdot d\alpha + \frac{\pi \cdot (\frac{\pi}{2} - \alpha_1)}{2 \cdot (1 - \sin \alpha_1)} \cdot \delta_b \cdot \tan \theta + (\frac{\pi}{2} - \alpha_1) \cdot \delta_s \right] \cdot a_g^2 \cdot \tan^2 \theta \end{aligned} \quad (19)$$

3.4 Force model of cutting and ploughing grain

Material behavior in ploughing stage could be categorized as plastic flow, in which stress should reach at δ_s . Therefore, force model of ploughing grain could be calculated as Eqs. (20) and (21).

$$F_{ip}(a_g) = \int_0^{\frac{\pi}{2}} \delta_s \cdot a_g^2 \cdot \tan \theta \cdot \cos \alpha \cdot d\alpha \quad (20)$$

$$F_{np}(a_g) = \int_0^{\frac{\pi}{2}} \delta_s \cdot a_g^2 \cdot \tan^2 \theta \cdot d\alpha = \frac{\pi}{2} \cdot \delta_s \cdot a_g^2 \cdot \tan^2 \theta \quad (21)$$

3.5 Frictional force model

The frictional force is composed of rake face on ploughing grains $F_{pf}(a_g)$, rake face on cutting grains $F_{cf}(a_g)$, and the wear plane of the grain (f_n, f_t), as shown in Eqs. (22)–(30). The force magnitude is determined by stress and the lubricating state between the grains and the workpiece.

$$F_{pf}(a_g) = 2 \cdot \int_0^{\frac{\pi}{2}} \mu \cdot \delta_s \cdot ds = \int_0^{\frac{\pi}{2}} \mu \cdot \delta_s \cdot a_g^2 \cdot \frac{\tan \theta}{\cos \theta} \cdot d\alpha \quad (22)$$

$$F_{ipf}(a_g) = F_{pf}(a_g) \cdot \sin \theta = \int_0^{\frac{\pi}{2}} \mu \cdot \delta_s \cdot a_g^2 \cdot \tan^2 \theta \cdot d\alpha \quad (23)$$

$$F_{nfp}(a_g) = F_{pf}(a_g) \cdot \cos \theta = \int_0^{\frac{\pi}{2}} \mu \cdot \delta_s \cdot a_g^2 \cdot \tan \theta \cdot d\alpha \quad (24)$$

$$\begin{aligned} F_{cf}(a_g) &= 2 \cdot \left(\int_{\alpha_1}^{\frac{\pi}{2}} \mu \cdot \delta_0 \cdot ds + \int_0^{\alpha_1} \mu \cdot \delta_1 \cdot ds \right) \\ &= \int_{\alpha_1}^{\frac{\pi}{2}} \mu \cdot \delta_0 \cdot a_g^2 \cdot \frac{\tan \theta}{\cos \theta} \cdot da + \int_0^{\alpha_1} \mu \cdot \delta_1 \cdot a_g^2 \cdot \frac{\tan \theta}{\cos \theta} \cdot da \end{aligned} \quad (25)$$

$$F_{tcf}(a_g) = F_{cf}(a_g) \cdot \sin \theta = \int_{\alpha_1}^{\frac{\pi}{2}} \mu \cdot \delta_0 \cdot a_g^2 \cdot \frac{\tan \theta}{\cos \theta} \cdot da + \int_0^{\alpha_1} \mu \cdot \delta_1 \cdot a_g^2 \cdot \frac{\tan \theta}{\cos \theta} \cdot da \quad (26)$$

$$F_{nfc}(a_g) = F_{cf}(a_g) \cdot \cos \theta = \int_{\alpha_1}^{\frac{\pi}{2}} \mu \cdot \delta_0 \cdot a_g^2 \cdot \tan \theta \cdot da + \int_0^{\alpha_1} \mu \cdot \delta_1 \cdot a_g^2 \cdot \tan \theta \cdot da \quad (27)$$

$$f_n = N_d \cdot S_w \cdot \bar{p} = \frac{4 \cdot P_0 \cdot S_w \cdot N_d \cdot V_w}{V_s \cdot D} = \frac{4 \cdot K_1 \cdot N_d \cdot V_w}{V_s \cdot D} \quad (28)$$

$$f_t = \mu \cdot N_d \cdot S_w \cdot \bar{p} = \frac{4 \cdot \mu \cdot P_0 \cdot \delta \cdot N_d \cdot V_w}{V_s \cdot D} = \frac{4 \cdot \mu \cdot K_1 \cdot N_d \cdot V_w}{V_s \cdot D} \quad (29)$$

$$K_1 = P_0 \cdot S_w \quad (30)$$

where K_1 is the physical quantity related to the grain's wear state of the grinding wheel, which could be reversely solved through grinding experiment, and μ is the friction coefficient between the workpiece and the grains, which could be obtained by tribological tests [40].

4. Grinding force model and prediction

4.1 Procedure of modeling common grinding wheel

The matrix of the location distribution of the grains in the grinding zone is established as $G(z_g)$. The matrix of the protrusion height of the grains can be calculated as [40]:

$$G(z) = \frac{G(d)}{2} + G(z_g) = \begin{bmatrix} z_{11} & z_{12} & \cdots & z_{1N_y} \\ z_{21} & z_{22} & \cdots & z_{2N_y} \\ \vdots & \vdots & \ddots & \vdots \\ z_{N_x1} & z_{N_x1} & \cdots & z_{N_xN_y} \end{bmatrix} \quad (31)$$

4.2 Dynamic active grains in grinding zone

For two continuous cutting grains, maximum undeformed chip thickness $a_{g\max}$ ($a_g = 0.5a_{g\max}$ [42]) could be solved as [41, 42]:

$$a_{g\max} = 2 \cdot \lambda \cdot \frac{V_w}{V_s} \cdot \sqrt{\frac{a_p}{D}} \quad (32)$$

where λ is the space between the continuous cutting grains, D is the diameter of the grinding wheel, V_w is the feed speed, and V_s is the peripheral speed of the grinding wheel.

For common grinding wheel, λ value represented the space between the dynamic active grains. The equation of the n th grain is deduced as:

$$a_{g\max(n)} = 2 \cdot \lambda_{(n \sim n-1)} \cdot \frac{V_w}{V_s} \cdot \sqrt{\frac{a_p}{D}} + (a_{p(n)} - a_{p(n-1)}) \quad (33)$$

where $a_{g\max(n)}$ is the maximum undeformed chip thickness of the n th dynamic active grain, $\lambda_{(n \sim n-1)}$ is the space between the n th and the $(n - 1)$ th dynamic active grains, $a_{p(n)}$ is the protrusion height of the n th dynamic active grain, and $a_{p(n - 1)}$ is the protrusion height of the $(n - 1)$ th dynamic active grain.

4.3 Grinding force model

Concrete calculation of grinding force can be described in **Figure 13**; the grinding force can be expressed in Eqs. (34) and (35).

$$F_t = \sum_1^{N_c} [F_{tc}(a_{gn}) + F_{tcf}(a_{gn})] + \sum_1^{N_p} [F_{tp}(a_{gm}) + F_{tpf}(a_{gm})] + f_t \quad (34)$$

$$F_n = \sum_1^{N_c} [F_{nc}(a_{gn}) - F_{ncf}(a_{gn})] + \sum_1^{N_p} [F_{np}(a_{gm}) - F_{npf}(a_{gm})] + f_n \quad (35)$$

where F_t/F_n are the tangential/normal grinding force, respectively, and f_t/f_n are the tangential/normal frictional force on the wear plane of grains, respectively. For the n th cutting grains ($1 \leq n \leq N_c$), a_{gn} is the cutting depth; $F_{tc}(a_{gn})/F_{nc}(a_{gn})$ are the tangential/normal cutting force, respectively; and $F_{tcf}(a_{gn})/F_{ncf}(a_{gn})$ are the tangential/normal frictional force on the rake face of the cutting grain, respectively. For the m th ploughing grains ($1 \leq n \leq N_c, N_c + N_p = N_d$), a_{gm} is the cutting depth; $F_{tp}(a_{gm})/F_{np}(a_{gm})$ are the tangential/normal, respectively; and $F_{tpf}(a_{gm})/F_{npf}(a_{gm})$ are the tangential/normal frictional force on the rake face of ploughing grain, respectively.

4.4 Experimental verification

MoS₂-palm oil nanofluid minimum quantity lubrication grinding experiment was carried out with K-P36 surface grinder. Prediction and experimental force values was shown in **Figure 14**.

The average percentage of the deviation in the normal force is 4.19%, while in the tangential force is 4.31%. For a certain grinding condition (dry grinding, $V_s = 20$ m/s, $V_w = 2$ m/min, $a_p = 15 \mu\text{m}$), the contribution of the tangential frictional force in the total tangential grinding force is approximately 89.17% and approximately 90.71% for normal force. However, it was decreased to 86.52% and 89.43% for tangential and normal direction, respectively.

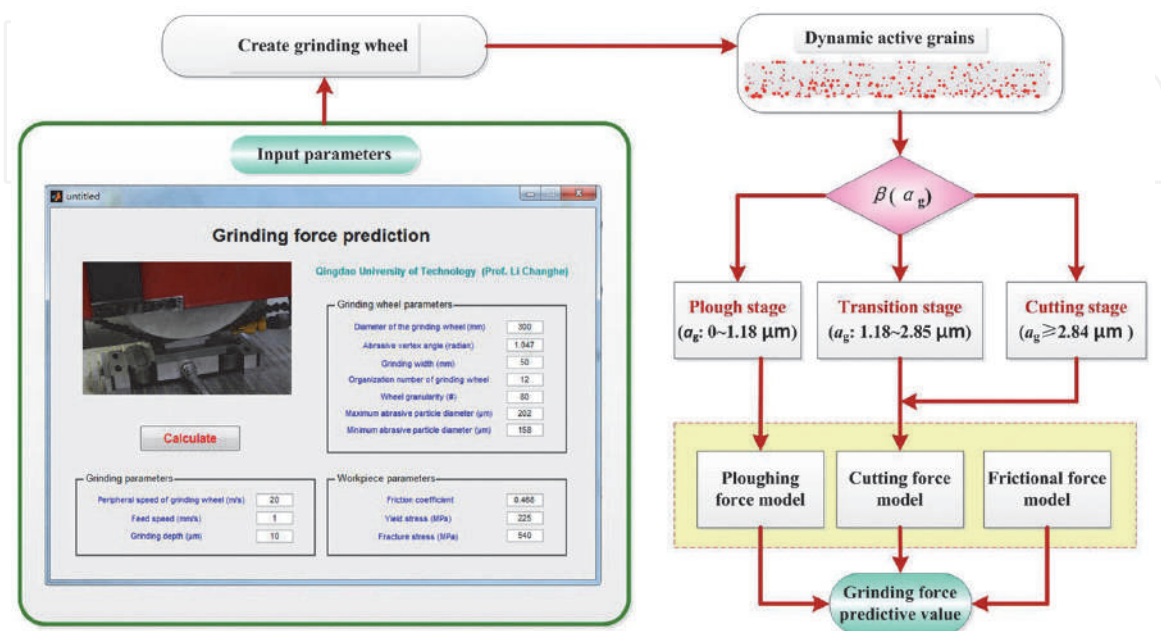


Figure 13.
 Process of the grinding force predictive program.

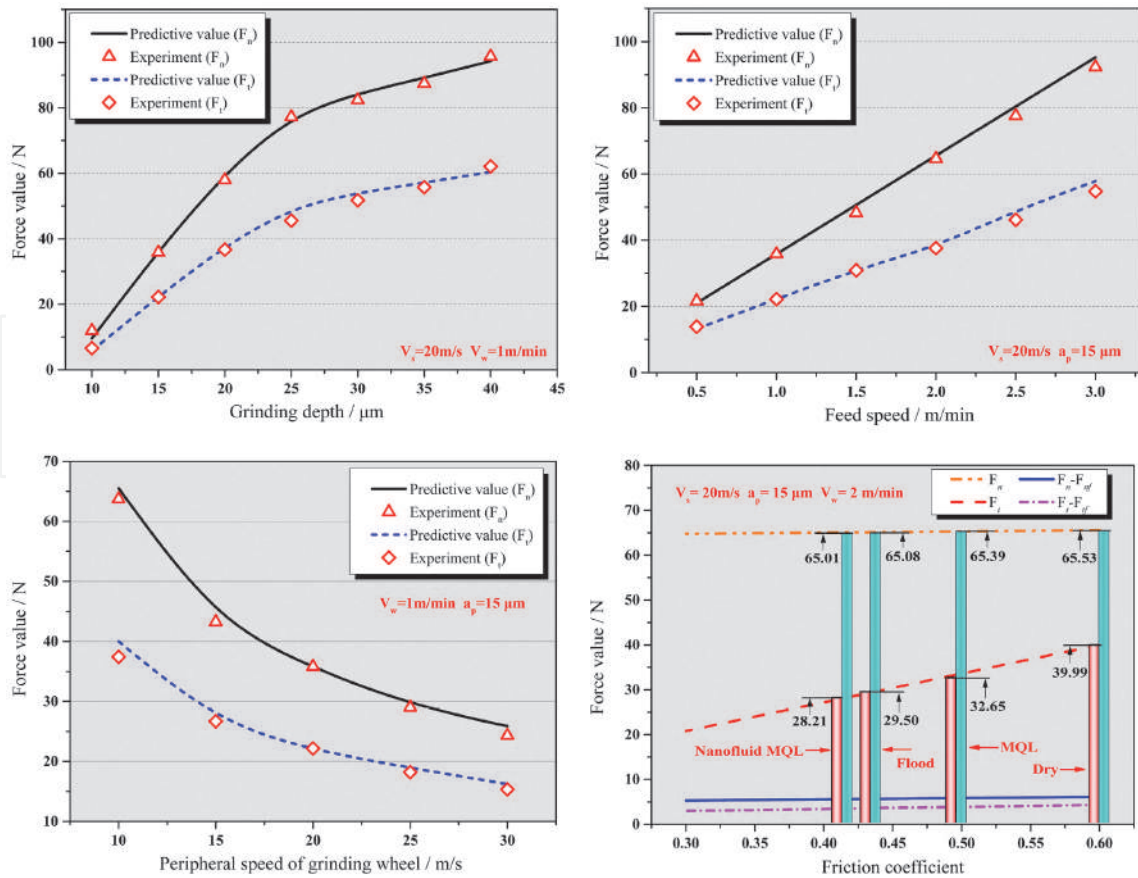


Figure 14.
Force prediction and experiment result.

5. Conclusions

To develop a model based on the stress state of a single grain, this study investigated the material removal mechanism and interference action in the grinding zone. The combined effect of the material removal and plastic stacking of a single grain has been considered.

Cutting experiment of single grain was carried out to obtain the critical cutting depth of the cutting and ploughing states. Results indicated that the variation trend of the grain-cutting efficiency (β) presents an S-shaped trend as the cutting depth (a_g) increases.

This study also developed and verified an improved grinding force predictive model. The average percentage of the deviation in the normal force is 4.19%, whereas that in the tangential force is 4.31%.

Acknowledgements

This research was financially supported by the following organizations: the National Natural Science Foundation of China (51975305 and 51905289), the Major Research Project of Shandong Province (2019GGX104040, 2019GSF108236, and 2018GGX103044), and the Shandong Provincial Natural Science Foundation of China (ZR2019PEE008), Major Science and technology innovation engineering projects of Shandong Province (2019JZZY020111), Applied basic research Youth Project of Qingdao science and technology plan (19-6-2-63-cg).

Conflict of interest

The authors declare no conflict of interest.

IntechOpen

Author details

Yanbin Zhang^{1,2}, Changhe Li^{1*}, Yongjun Zhao^{2*}, Xin Cui¹, Xiufang Bai³,
Mingzheng Liu¹, Yali Hou¹, Min Yang¹, Naiqing Zhang⁴, Heju Ji⁵, Xiaoming Wang¹
and Teng Gao¹

1 School of Mechanical Engineering, Qingdao University of Technology, Qingdao, China

2 MH Robot and Automation Co., Ltd., Weifang, China

3 School of Mechanical and Electrical Engineering, Qingdao Binhai University, Qingdao, China

4 Shanghai Jinzhao Energy Saving Technology Co. Ltd., Shanghai, China

5 Qingdao Dong Jia Textile Machinery Group Co., Ltd., Qingdao, China

*Address all correspondence to: sy_lichanghe@163.com; 18622115276@163.com

IntechOpen

© 2020 The Author(s). Licensee IntechOpen. Distributed under the terms of the Creative Commons Attribution - NonCommercial 4.0 License (<https://creativecommons.org/licenses/by-nc/4.0/>), which permits use, distribution and reproduction for non-commercial purposes, provided the original is properly cited. 

References

- [1] Zhang YB, Li CH, Jia DZ, et al. Experimental evaluation of the lubrication performance of MoS₂/CNT nanofluid for minimal quantity lubrication in Ni-based alloy grinding. *International Journal of Machine Tools & Manufacture*. 2015;**99**:19-33. DOI: 10.1016/j.ijmachtools.2015.09.003
- [2] Yang M, Li CH, Zhang YB, et al. Research on microscale skull grinding temperature field under different cooling conditions. *Applied Thermal Engineering*. 2017;**126**:525-537. DOI: 10.1016/j.applthermaleng.2017.07.183
- [3] Jia DZ, Li CH, Zhang YB, et al. Experimental evaluation of surface topographies of NMQL grinding ZrO₂ ceramics combining multiangle ultrasonic vibration. *The International Journal of Advanced Manufacturing Technology*. 2019;**100**(1-4):457-473. DOI: 10.1007/s00170-018-2718-y
- [4] Wu WT, Li CH, Yang M, et al. Specific Energy and G ratio of Grinding Cemented Carbide under Different Cooling and Lubrication Conditions. *The International Journal of Advanced Manufacturing Technology*. 2019;**105**(1-4):67-82. DOI: 10.1007/s00170-019-04156-5
- [5] Wang YG, Li CG, Zhang YB, et al. Comparative evaluation of the lubricating properties of vegetable-oil-based nanofluids between frictional test and grinding experiment. *Journal of Manufacturing Processes*. 2017;**26**:94-104. DOI: 10.1016/j.jmapro.2017.02.001
- [6] Li HN, Xie KG, Wu B, Zhu WQ. Generation of textured diamond abrasive tools by continuous-wave CO₂ laser: Laser parameter effects and optimisation. *Journal of Materials Processing Technology*. 2020;**275**:116279. DOI: 10.1016/j.jmatprotec.2019.116279
- [7] Li HN, Yang Y, Zhao YJ, et al. On the periodicity of fixed-abrasive planetary lapping based on a generic model. *Journal of Manufacturing Processes*. 2019;**44**:271-287. DOI: 10.1016/j.jmapro.2019.05.036
- [8] Gao T, Zhang XP, Li CH, et al. Surface morphology evaluation of multi-angle 2D ultrasonic vibration integrated with nanofluid minimum quantity lubrication grinding. *Journal of Manufacturing Processes*. 2020;**51**:44-61. DOI: 10.1016/j.jmapro.2020.01.024
- [9] Zhang YB, Li CH, Jia DZ, et al. Experimental evaluation of MoS₂ nanoparticles in jet MQL grinding with different types of vegetable oil as base oil. *Journal of Cleaner Production*. 2015;**87**:930-940. DOI: 10.1016/j.jclepro.2014.10.027
- [10] Yang M, Li CH, Zhang YB, et al. Predictive model for minimum chip thickness and size effect in single diamond grain grinding of zirconia ceramics under different lubricating conditions. *Ceramics International*. 2019;**45**(12):14908-14920. DOI: 10.1016/j.ceramint.2019.04.226
- [11] Yang M, Li CH, Zhang YB, et al. Maximum undeformed equivalent chip thickness for ductile-brittle transition of zirconia ceramics under different lubrication conditions. *International Journal of Machine Tools and Manufacture*. 2017;**122**:55-65. DOI: 10.1016/j.ijmachtools.2017.06.003
- [12] Werner G. Influence of work material on grinding forces. *CIRP Annals*. 1978;**27**:243-248
- [13] Malkin S, Hwang TW. Grinding mechanisms for ceramics. *CIRP Annals*. 1996;**45**(2):569-580. DOI: 10.1016/S0007-8506(07)60511-3
- [14] Li L, Fu J, Peklenik J. A study of grinding force mathematical model.

- CIRP Annals. 1980;**29**(1):245-249. DOI: 10.1016/S0007-8506(07)61330-4
- [15] Younis M, Sadek MM, El-Wardani T. A new approach to development of a grinding force model. *Journal of Engineering Industry*. 1987;**109**(4): 306-313
- [16] Tang J, Du J, Chen Y. Modeling and experimental study of grinding forces in surface grinding. *Journal of Materials Processing Technology*. 2009;**209**(6): 2847-2854. DOI: 10.1016/j.jmatprotec.2008.06.036
- [17] Hecker RL, Liang SY, Wu XJ, et al. Grinding force and power modeling based on chip thickness analysis. *The International Journal of Advanced Manufacturing Technology*. 2007;**33**(5-6):449-459. DOI: 10.1007/s00170-006-0473-y
- [18] Lang X, He Y, Tang J, et al. Grinding force model based on prominent height of abrasive submitted to Rayleigh distribution. *Journal of Central South University (Science and Technology)*. 2014;**45**(10):3386-3391
- [19] Zhang J, Ge P, Zhang L. Research on the grinding force based on the probability statistics. *China Mechanical Engineering*. 2007;**18**(20): 2399-2402
- [20] Chang CH, Wang J-JJ. A stochastic grinding force model considering random grit distribution. *International Journal of Machine Tools and Manufacture*. 2008;**48**(12-13): 1335-1344. DOI: 10.1016/j.ijmachtools.2008.05.012
- [21] Cheng J, Wu J, Gong YD, et al. Grinding forces in micro slot-grinding (MSG) of single crystal sapphire. *International Journal of Machine Tools and Manufacture*. 2017;**112**:7-20. DOI: 10.1016/j.ijmachtools.2016.10.004
- [22] Zhou M, Zheng W. A model for grinding forces prediction in ultrasonic vibration assisted grinding of SiCp/Al composites. *The International Journal of Advanced Manufacturing Technology*. 2016;**87**(9-12):3211-3224. DOI: 10.1007/s00170-016-8726-x
- [23] Jiang Z, Yin Y, Wang Q, et al. Predictive modelling of grinding force considering wheel deformation for toric optical mirrors. *Journal of Manufacturing Science and Engineering*. 2016;**138**(6):061008. DOI: 10.1115/1.4032084
- [24] Li HN, Yu TB, Wang ZX, et al. Detailed modeling of cutting forces in grinding process considering variable stages of grain-workpiece micro interactions. *International Journal of Mechanical Sciences*. 2017;**126**:319-339. DOI: 10.1016/j.ijmecsci.2016.11.016
- [25] Younis MA, Alawi H. Probabilistic analysis of the surface grinding process. *Transactions of the Canadian Society for Mechanical Engineering*. 1984;**8**(4): 208-213. DOI: 10.1139/tcsme-1984-0031
- [26] Zhang Y, Li C, Yang M, et al. Experimental evaluation of cooling performance by friction coefficient and specific friction energy in nanofluid minimum quantity lubrication grinding with different types of vegetable oil. *Journal of Cleaner Production*. 2016;**139**: 685-705. DOI: 10.1016/j.jclepro.2016.08.073
- [27] Cui X, Li C, Zhang Y, Jia D, Zhao Y, Li R, et al. Tribological properties under the grinding wheel and workpiece interface by using graphene nanofluid lubricant. *The International Journal of Advanced Manufacturing Technology*. 2019;**104**(9-12):3943-3958. DOI: 10.1007/s00170-019-04129-8
- [28] Zhang ZY, Wang B, Kang RK, et al. Changes in surface layer of silicon wafers from diamond scratching. *CIRP Annals*. 2015;**64**(1):349-352. DOI: 10.1016/j.cirp.2015.04.005

- [29] Cao JG, Wu YB, Li JY, et al. A grinding force model for ultrasonic assisted internal grinding (UAIG) of SiC ceramics. *The International Journal of Advanced Manufacturing Technology*. 2015;**81**(5-8):875-885. DOI: 10.1007/s00170-015-7282-0
- [30] Zhang Z, Guo D, Wang B, et al. A novel approach of high speed scratching on silicon wafers at nanoscale depths of cut. *Scientific Reports*. 2015;**5**:16395. DOI: 10.1038/srep16395
- [31] Zhang Z, Guo L, Cui J, et al. Nanoscale solely amorphous layer in silicon wafers induced by a newly developed diamond wheel. *Scientific Reports*. 2016;**6**:35269. DOI: 10.1038/srep35269
- [32] Zhang J, Song Y, Huo F, et al. Nanoscale material removal mechanism of soft-brittle HgCdTe single crystals under nanogrinding by ultrafine diamond grits. *Tribology Letters*. 2012;**46**(1):95-100. DOI: 10.1007/s11249-012-9924-9
- [33] Ding W, Dai J, Zhang LC, et al. An investigation on the chip formation and forces in the grinding of Inconel718 alloy using the single-grain method. *Issues in Mental Health Nursing*. 2014;**28**:1-2. DOI: 10.1016/j.ijmachtools.2017.06.002
- [34] Jin T, Stephenson DJ. Heat flux distributions and convective heat transfer in deep grinding. *International Journal of Machine Tools and Manufacture*. 2006;**46**(14):1862-1868. DOI: 10.1016/j.ijmachtools.2005.11.004
- [35] Zhang J, Wang Y, Wang Y. Experiment and constitutive model of rate-dependent behavior of titanium alloy TC11. *The Chinese Journal of Nonferrous Metals*. 2017;**27**(07):1369-1375. DOI: 10.19476/j.ysxb.1004.0609.2017.07.07
- [36] Xun C, Rowe WB. Analysis and simulation of the grinding process. Part II: Mechanics of grinding. *International Journal of Machine Tools and Manufacture*. 1996;**36**(8):883-896. DOI: 10.1016/0890-6955(96)00117-4
- [37] Du HJ, Rui YN, Wang R, et al. MATLAB-based simulation method of surface's three-dimensional model in grinding process. *Modern Manufacturing Engineering*. 2009;(02):48-51. DOI: CNKI:SUN:XXGY.0.2009-02-013
- [38] Öpöz TT, Chen X. Effect of different parameters on grinding efficiency and its monitoring by acoustic emission. *Production & Manufacturing Research*. 2016;**4**(1):190-208. DOI: 10.1080/21693277.2016.1255159
- [39] Lindsay RP, Hahn RS. *Principle of Grinding, Part I, II*. Machinery. 1971
- [40] Zhang Y, Li C, Ji H, et al. Analysis of grinding mechanics and improved predictive force model based on material-removal and plastic-stacking mechanisms. *International Journal of Machine Tools and Manufacture*. 2017;**122**:81-97. DOI: 10.1016/j.ijmachtools.2017.06.002
- [41] Agarwal S, Venkateswara Rao P. Predictive modeling of force and power based on a new analytical undeformed chip thickness model in ceramic grinding. *International Journal of Machine Tools and Manufacture*. 2013;**65**:68-78. DOI: 10.1016/j.ijmachtools.2012.10.006
- [42] Cai R, Qi HS, Cai GQ. Active cutting edges in vitrified CBN grinding wheels. *Key Engineering Materials*. 2006;**304**:1-7. DOI: 10.4028/www.scientific.net/KEM.304-305.1